TITLE:

The normal human lymph node cell classification and landscape defined by high-dimensional spatial proteomic.

Short title: Lymph node landscape and cell classification

Authors:
Maddalena M Bolognesi[1,2 †], Lorenzo Dall'Olio[3 †], Giulio Eugenio Mandelli[4,5], Luisa Lorenzi[4,5], Francesca M Bosisio[6,7,8], Ann M Haberman[9,10], Govind Bhagat[11¶], Simone Borghesi[12], Mario Faretta[13], Gastone Castellani[14 †] and Giorgio Cattoretti[15 †*]

Affiliations:
1 Istituto di Bioimmagini e Sistemi Biologici Complessi (IBSBC) – CNR Via F.lli Cervi, 93 20090 Segrate (MI).
2 NBFC, National Biodiversity Future Center, Palermo 90133, Italy.
3 Laboratorio di Data Science and Bioinformatics, IRCCS Istituto delle Scienze Neurologiche di Bologna – AUSL BO Ospedale Bellaria, Via Altura 3 - 40139 Bologna - Italy.
4 Pathology Unit, Department of Molecular and Translational Medicine-DMMT, University of Brescia, via Branze, 43, 25123 Brescia, Italy.
5 Pathology Unit, ASST Spedali Civili Di Brescia, Brescia,Italy.
6 The Leuven Institute for Single-cell Omics (LISCO), KULeuven, Leuven, Belgium.
7 Translational Cell and Tissue Research Unit, Department of imaging and pathology, KULeuven, Leuven, Belgium.
8 Pathology Department, University Hospital of Leuven, Leuven, Belgium.
9 Department of Immunobiology, Yale University, New Haven, Connecticut, USA.
10Department of Laboratory Medicine, Yale University, New Haven, Connecticut, USA.
11 Columbia University Irving Medical Center and New York Presbyterian Hospital, NewYork, NY, USA.
12 Department of Mathematics and Applications, University of Milano Bicocca, 20126 Milan, Italy.
13 Department of Experimental Oncology, European Institute of Oncology IRCCS, 20139 Milan, Italy
14 Department of Experimental, Diagnostic and Specialty Medicine, University of Bologna, 40127 Bologna, Italy.
15 Pathology, Department of Medicine and Surgery, Universitá di Milano-Bicocca, 20900 Monza (MI), Italy.

† These authors contributed equally to this work
¶ present address: Pathology, Saint Louis University School of Medicine, Saint Louis, MO, USA

*Correspondence: giorgio.cattoretti@unimib.it

TABLE OF CONTENTS (has links)

ABSTRACT 4

MAIN TEXT 5

INTRODUCTION 5

RESULTS 5

T-cells, CD4 and CD8 7

B-cells and plasma cells 11

Innate immune and dendritic cells 14

Myelomonocytic cells 17

Non-hematopoietic stromal cells identified in normal LN 19

Neighborhoods of the normal human LN 20

The landscape of the normal human LN 22

DISCUSSION 24

LIMITATIONS OF THE STUDY 27

MATERIALS AND METHODS 28

EXPERIMENTAL DESIGN 28

Human specimens 28

METHOD DETAILS 28

Tissue Microarray (TMA) preparation 28

Histology repository 28

Anatomical terms and definitions 29

Antigen retrieval 29

Antibody validation and staining 29

MILAN Immunofluorescence 29

Preparation of immunofluorescent images for single cell analysis. 30

Validation of the analytical pipeline 30

Cell segmentation 30

Artifact identification and subtraction with BRAQUE 30

Antibody panel high dimensional validation 30

Sample size representativeness 31

Iconographic rendering 31

QUANTIFICATION AND STATISTICAL ANALYSIS 31

High dimensional analysis with BRAQUE 31

BRAQUE preprocessing 32
Gaussian Mixture Components: 32
BRAQUE nested classification: 32
Minimum size of cell group: 32
BRAQUE data output and analysis 33
Post-classification data analysis 33
Neighborhood analysis 33
Overlap 34
Fisher significance test 35
Distance 35
Significance of zonal distribution of cell subsets across zones. 35
REFERENCES AND NOTES 36
ACKNOWLEDGMENTS 48
FUNDING 48
AUTHOR CONTRIBUTIONS 48
COMPETING INTERESTS 49
DATA AND MATERIALS AVAILABILITY 49
Declaration of generative AI and AI-assisted technologies 49
FIGURES AND TABLES 49
FIGURE LEGENDS 49
TABLE LEGEND 53

ABSTRACT

Lymph nodes (LN) are key secondary lymphoid organs (SLO) for a coordinated immune response. They have been extensively characterized by numerous investigative techniques chiefly as single cell suspensions because they are composed of vagile yet crowded hematolymphoid elements, unfriendly to spatial tissue organization-saving techniques. We comprehensively classify in situ all cells of 19 human LN free of pathology with a 78-marker antibody panel, an hyperplexed cyclic staining method, MILAN, and an analytical bioinformatic pipeline, BRAQUE. A total of 77 cell types were classified encompassing T, B, innate immune and stromal cells. By leveraging the expression profiles of TCF7 and co-inhibitory receptor distribution, CD4 and CD8 T-cells were classified into 27 subsets with distinct phenotypes and tissue locations. CD5 and TCF7 expression defined novel B-cell types. CD27+ mature B-cells occupied novel nodal spaces non-overlapping with the cortex and the plasma-cell rich medullary cords. Type 2 conventional dendritic cells were located in nodular paracortical aggregates. Statistically controlled pairwise neighborhood analysis showed sparse cell-cell interactions, known and new neighbors, established and novel LN landscape niches. A high-dimensional proteomic interrogation of the normal human LN provides spatial allocation of known cell types, novel interactions and the landscape organization.

MAIN TEXT

INTRODUCTION

The anatomical structure of the lymph node (LN)[1] is instrumental for its function, primarily to promote the interactions of cells with antigens or other cell types within discrete niches[2]. These interactions have been extensively studied in-vivo in mice and ex-vivo in humans, recently with high-capacity methods at the single cell level, determining the transcriptomes or any other genetic or epigenetic aspects, providing a view of the immune system in unprecedented detail. Such studies have produced a granular classification of the immune cells in various organs, including the LN, and along human immune system development[3], with some investigations specifically focusing on individual cell types[4]. The common goal of these initiatives is to build a Human Cell Atlas[5] to be used as a framework for a better knowledge of normal tissue architecture and cellular function in its tissue context that could potentially help in the development of novel therapies for a variety of diseases.

Starting in the 80's, in situ immunostaining techniques have contributed to establish a static view of the immune architecture of the human LN; more recently, the use of various methods for the detection of multiple antigens at once[6] have provided a topographic view of the immune response, both for hematopoietic[7, 8] and non-hematopoietic LN cells[9]. However, the global spatial cell composition of the LN has not been fully elucidated as a whole with in-situ methods. We undertook a spatial single cell classification of a large number of LNs, representing variegated aspects of normalcy, with a panel of 78 antibodies and a novel image analytical pipeline, BRAQUE[10]. We here provide a granular purely phenotypic classification of established and novel cell types populating the human LN. We then established the relationships of each cell type with the others via a robust statistical approach and, lastly, we defined the regional landscape of the human lymph node based on the selective distribution of neighboring or distant cell types. In such a way we provide a reference database from which to extrapolate the effects of sustained immune challenges or neoplastic transformation.

RESULTS

To classify all cell types composing six whole LN sections and 36 duplicate 2mm tissue cores from 19 LN (Table S1), for a total of 7,500,552 cells (5,891,960 cells in the six whole sections), we stained them in saturating conditions[11] with 78 antibodies (Figure 1A, Figure S1 and Table S2) according to the MILAN method[12]. We then developed and applied an analytical pipeline, BRAQUE, consisting of a bundled segmentation algorithm (CyBorgh), a preprocessing phase to

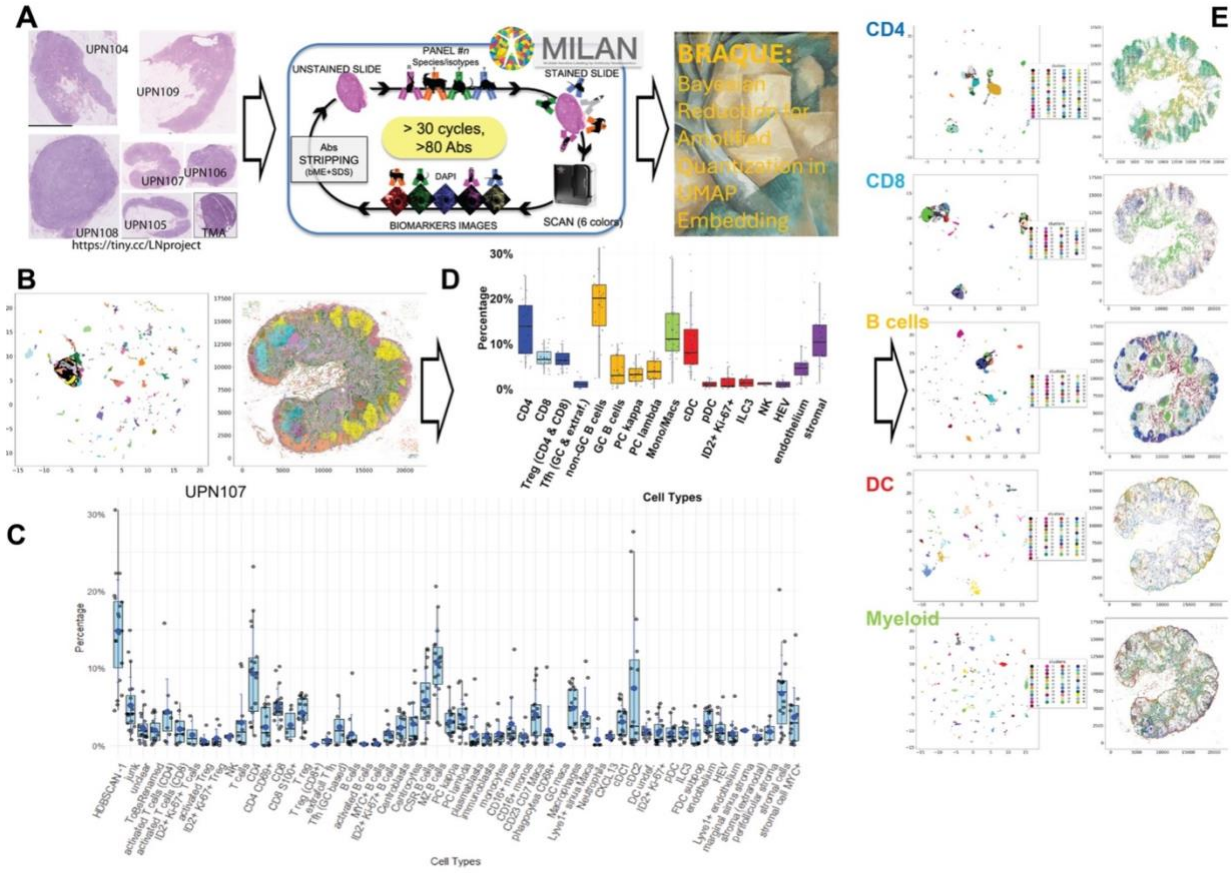

Figure 1

Global single cell classification by BRAQUE in tissue sections.

A: The BRAQUE analysis pipeline. Right: sections of whole LN H&E images (WSI; scale bar = 5 mm. The TMA core, black image border, has a diameter of 2 mm). The images can be examined at the link to https://tiny.cc/LNproject.The cartoon at the center depicts the cyclic staining and stripping MILAN method, followed by BRAQUE.

B: The UMAP virtual 2D map (left) and the real spatial distribution (right) of 727,729 cells, clustered with BRAQUE^{global}, is shown. Each cluster is color-coded. The scale on the left is virtual, the scale on the right are pixels (0.45µm/pixels). Case: UPN107.

C: The cell types identified in 27 LN samples (6 whole LN and 21 2mm TMA cores) after BRAQUE^{global} analysis on all cells in each sample, expressed as boxplots delimited by interquantile ranges, containing the median value (bar) and the mode (asterisk), whiskers indicating min/max values and individual sample points, including outliers. Data are reported in Table S3.

D: The cell types identified in C are grouped as broad cell types, expressed as boxplots (see specification in Fig1C), excluded HDBSCAN -1, junk and unclassified from the calculation. Data are reported in Table S3.

E: The broad categories of CD4, CD8, B cells, dendritic and non-myeloid innate cells (DC) and myeloid cells shown in color in D was each separately analyzed by BRAQUE^{subclass} and each UMAP shown for UPN107 as an example. Images specifications are as per B.

enhance cluster separation (called Lognormal Shrinkage), a dimensionality reduction algorithm (UMAP), and a clustering algorithm (HDBSCAN)[10].
BRAQUE is able to identify clusters composed of as little as 12 cells and comprising down to 0.01% of total sample cells (Table S3); however for maximal detail we applied a two-step, nested application of BRAQUE to the segmented cells, i.e. a comprehensive BRAQUE^{global} classification (Figure 1B, 1C, Table S4, Table S3, Table S5) followed by a broad cell-type targeted BRAQUE^{subclassification} analyzing separately CD4 and CD8 T-cells, B-cells, myeloid cells and non-myeloid dendritic cells (Figure 1D, 1E)(Table S6). In total, this pipeline produced a 77 cell type classification of the 6 human whole LN samples (Table S7).
These phenotypic cell types (interchangeably named phenotypic "subsets") are illustrated below.

T-cells, CD4 and CD8

The cell fate of mature T-cells is dictated by the presence and activity of TCF7, a transcription factor (TF) that provides stem cell-like properties and flexible adaptation[13, 14]. TCF7 levels correspond to a time-dependent sequence of activation and resolution of an immune challenge[15], thus we arbitrarily divided T-cells stratified by their TCF7 expression into high, low and average levels (Figure 2A).
No consistent phenotype was produced by classifying T-cells based on TCF7 expression alone (Table 1); therefore we used the expression levels of TCF7, the presence of FOXP3 and the co-expression of other markers (checkpoint inhibitors TIM3, PD1 and CD137; proliferation indicator Ki67 etc.) as a strategy to classify clusters of CD4 and CD8 cells (Table 1, Table S8)(Figure 2B, 2C), that resulted in the identification of 14 CD4 and 13 CD8 cell types (Figure 2C through K, Figure S5). The random selection of patient cases, for which any recent antigenic exposure was unknown, was reflected in the heterogeneity in T-cell subset composition in each LN (Figure 2 I, K, Figure S5), as well as for any other cell type.

We found that among CD4+ T-cells, FOXP3 and TCF7^{hi} cells were mutually exclusive and T_{regs} were about equally split between having TCF7^{average} and TCF7^{low} (Figure 2C). This was expected, given the suppressive effect of TCF7 on the FOXP3 gene expression[16]
In contrast, CD8+ T_{reg} never displayed low TCF7 levels, except when activated.
A portion of T_{regs}, both CD4 and CD8, co-expressed FOXP3 and ID2 (Table 1, Table S8), possible evidence of plasticity[17]. FOXP3+ CD4 and CD8 cells could be further subdivided

based on the presence of additional activation markers and PRDM1[18] (Table 1, Table S8)(Figure 2C). Proliferating and S100B+ T_{reg}s were also heterogeneous in amount and distribution (Figure 2I, K).

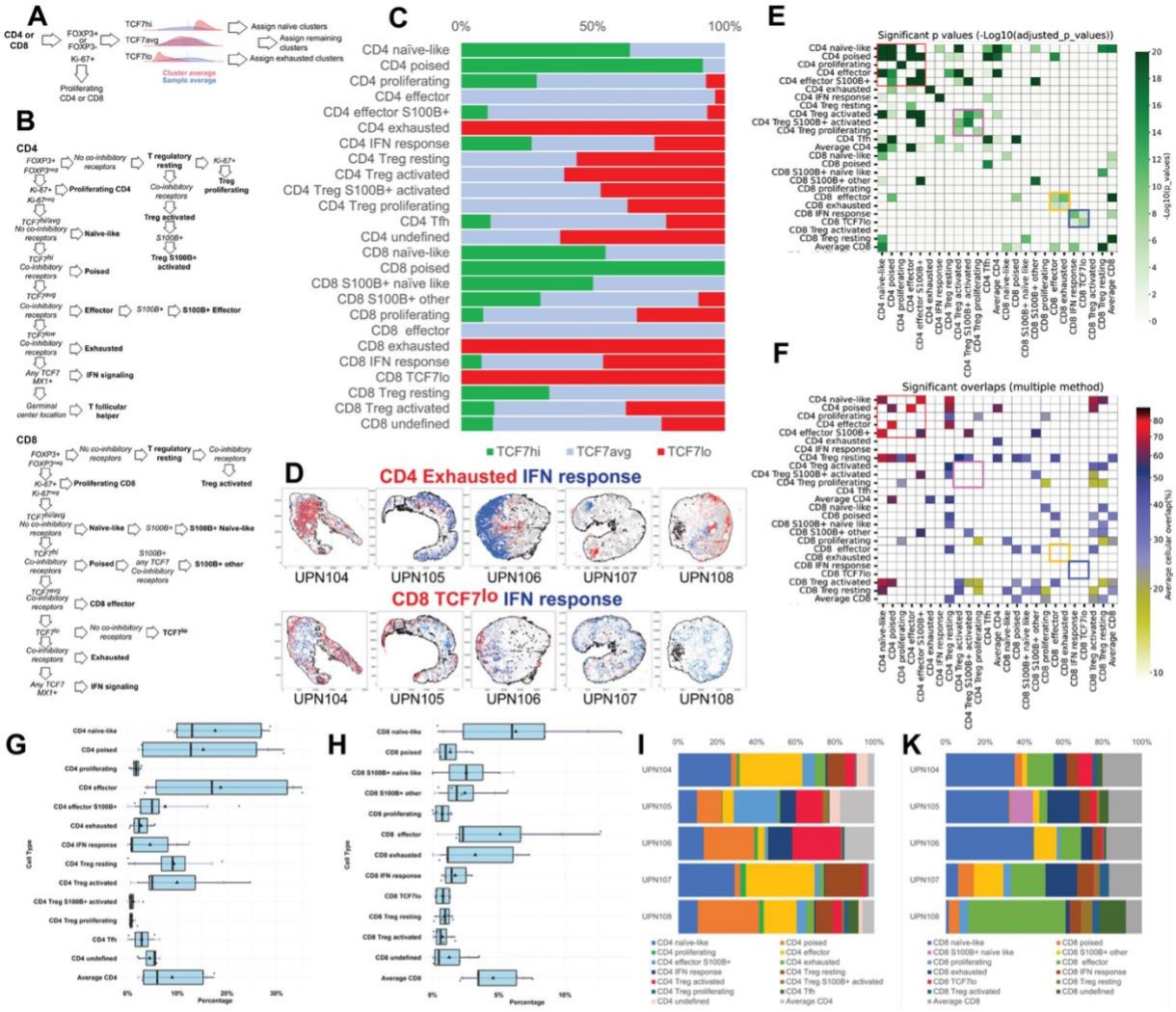

Figure 2

T-cell classification and spatial distribution

A: Flowchart for the assignment of the TCF7 level category. Non-proliferating CD4 or CD8 T-cells are classified based on high, low and intermediate levels of TCF7, as depicted by the cluster signal intensity profile (red), compared to the sample population (blue).

B: Flowchart for the assignment of the subset type for CD4 and CD8 T-cell clusters upon subclustering. The presence/absence of subclassifying markers is drawn from the BRAQUE statistical output (see[10,78])

C: Levels of TCF7 in CD4 and CD8 T-cell subsets. TCF7 levels (high, average or low) are plotted for each CD4 and CD8 cell subtypes as percentage of clusters belonging to a subtype having that level.

D: Examples of spatial co-localization of T-cell subsets in whole LN sections. CD4 exhausted (red dots) and CD4 IFN response T-cells (blue dots) are examples of cell types with non-overlapping distribution. CD8 TCF7lo (red dots) and CD8 IFN response T-cells (blue dots) are an example of neighboring cell types.

E: CD4 and CD8 neighborhood significant relationships. For each T-cell type the statistically significant neighbors are computed. Only significant values are plotted in shades of green as per the scale on the right. Note that CD4 with high or average TCF7 levels tend to be neighbors (red square). Activated and proliferating CD4 Treg, but not resting Treg also congregate together (pink square). CD8 effectors and exhausted are neighbors (orange square) as two CD8 subsets, CD8 TCF7lo and CD8 IFN signal do (blue square). Average CD4 and CD8 represents HDBSCAN -1 clusters. 518,116 CD4 and 190,365 CD8 cells analyzed. The complete neighborhood and overlap chart can be seen in Figure 6.

F: CD4 and CD8 subtypes significant overlaps. CD4 with high or average TCF7 levels occupy overlapping spaces in the whole LN (red square); scale on the right. Treg cell space, resting CD4 and activated or resting CD8, overlap with several other T-cell subsets. Note that previously noted (E) selected neighborhoods (pink, range and blue squares) do not correspond to spatial overlap regions.

G, H: CD4 and CD8 T-cells. T-cell types obtained after BRAQUE from five whole LNs represented as boxplots. For the boxplots specifications see Fig1.

I, K: CD4 and CD8 T-cell subtypes percentage composition of five whole lymph nodes.

The FOXP3-negative T-cells displayed a remarkable mirroring of phenotypic subtypes in CD4 and CD8 T-cells (Table 1, Table S8). Both CD4+ and CD8+ T-cells contained TCF7^{hi} cells expressing progenitor-associated markers (BCL6, GATA3, ID2 and PRDM1)[19, 20].
Both subsets also showed TCF7^{hi} cells with heterogeneous presence of checkpoint inhibitors listed above, cytotoxicity (GZMB) and activation markers (CD23); we defined these cells as being "poised" to acquire an effector phenotype[13, 21] or at a stage before transitioning to a TCF7^{low} phenotype[15, 22]. Resident memory CD4 T-cells (T_{rm}) may be the closest subset described[23].
We defined T-cells with average levels of TCF7 (lacking either high or low levels of this TF), displaying checkpoint inhibitors and activation markers as "effectors", also known as progenitors exhausted (T_{pex};[22]). They could be distinguished from TCF7^{low} cells, the latter bearing a more consistent phenotype (GZMB, CD137, PD1 etc.) and corresponding to "exhausted" T-cells[13].
Both CD4+ and CD8+ T-cells contained S100B+ subpopulations, a known naïve subset for CD8+ T-cells[24, 25]. In addition, S100B+ CD8+ T-cells with checkpoint inhibition and activation markers could be distinguished from naïve cells and had variable TCF7 levels.
S100B+ CD4+ subsets with an effector phenotype localized close to CD5+ conventional dendritic cells type 2 (cDC2) (Table 1, Table S8, Table S9 and Table S10). We could not define if this phenotype was due to a cell autonomous S100B+ phenotype[25] or because of proximity with a S100B+ DC with dendrites. We favor the first scenario because the phenotype of these T-cells did not completely match the repertoire of the neighboring DC.

Germinal Center (GC) based T follicular helper CD4+ T-cells (T_{fh}) clustered separately from the other CD4 cells and displayed the expected phenotypes (Table 1, Table S8). Remarkably, more than 50% of T_{fh} clusters, together with proliferating and activated T_{regs} and IFN-responsive CD8, contained cMAF, a TF crucial for T_{fh} differentiation[26].

Additionally, CD4+ and CD8+ T-cell subsets expressed MX1, a marker of interferon (IFN) signaling[4, 27, 28], had a mixed TCF7 profile but few other characterizing markers (Table 1, Table S8)(Figure S5): we defined them as "IFN response" T-cells[4, 29].
A population of CD8 T-cells featuring low TCF7 levels and few other characterizing markers (CD8 TCF7^{lo}) was found to colocalize and interact with CD8+ MX1+ cMAF+ IFN response T-cells (Figure 2D, E) (Table 1, Table S8, Table S9 and Table S10), suggesting a close functional relationship.

Proximity and likelihood of interaction of cell subsets were assessed using the novel Neighborhood and Overlap analyses. Briefly, statistically significant neighbors are computed for each cell subset using an odds ratio assessment of a cell type's location within/without a defined distance from another and the significance determined using the Fisher statistical test. With the more stringent Overlap analysis, the likelihood of a cell type being within a defined distance to cells of another type is expressed as a cellular overlap scale in which higher scores indicate a greater propensity for proximity. These analyses and their application to a broader collection of cell types are described in more detail further below.

B-cells and plasma cells

BRAQUE^{subclass} analysis produced 19 B-cell types, the spatial distribution of which landmarks the architecture of LNs without pathology. Some of the identified populations are phenotypically novel (Figure 3, Figure S6A).The markers used to classify each cell subset are listed in Table 1 and Table S8, and include IgD and CD27 to distinguish non-GC mature B cells and memory B cells (MBC) and those that have isotype switched (class switched recombined; CSR) [30, 31].

The phenotype and physical location of some subsets are noteworthy. Whereas CD27^{neg} B-cells, IgD+ or IgD^{neg}, had a follicular distribution, populating the MZ, all CD27+ B-cells had an almost completely mutually exclusive distribution and were located in the medullary cords or marginal to the B-cell follicles (Figure 3C, Figure S7).

CD5 expression defined 4 additional B-cell types, including one found in the periphery of the MZ and spilled into the paracortex(CD5+ MZ) (Figure 3E, Figure S6A). CD5+ T-zone B-cells instead were mainly confined within the T-cell zone (Figure 3E, Figure S6A) (Table 1, Table S8). The phenotype of these two CD5+ subsets was notable for the absence/low levels of restricted B-cell markers such as CD20 or CD79a (except IgD in 30-50% of CD5+ MZ clusters) and a TCF7^{low}, PAX5^{low} phenotype (Figure 3F, Figure S6A) (Table 1, Table S8, Table S11). Phenotypically, these clusters resemble the "transitional naïve B-cells"[32] or T1 B-cells[33, 34], i.e. IgD±, CD27^{neg}, CD43^{neg}, CD23^{neg}, rather than B1 cells (CD27+, CD43+, CD5±). CD5+ MZ and T-zone cell subsets were identified in about 40% of the LNs examined (Table S11) and in all cases in the same marginal follicular zone location.

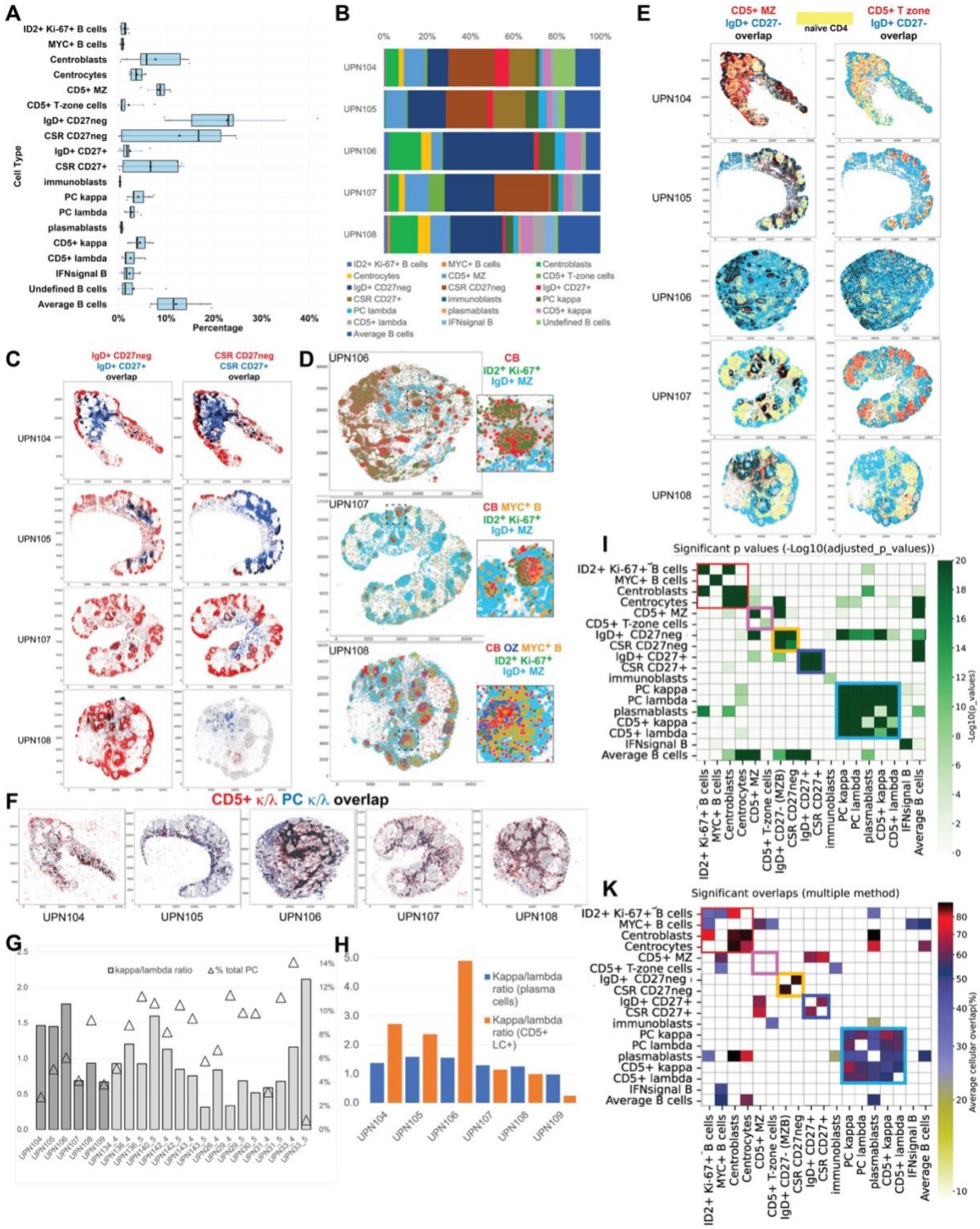
A
ID2+ Ki-67+ B cells
MYC+ B cells
Centroblasts
Centrocytes
CD5+ MZ
CD5+ T-zone cells
IgD+ CD27neg
CSR CD27neg
IgD+ CD27+
CSR CD27+
immunoblasts
PC kappa
PC lambda
plasmablasts
CD5+ kappa
CD5+ lambda
IFNsignal B
Undefined B cells
Average B cells
Cell Type
Percentage
B
UPN104
UPN105
UPN106
UPN107
UPN108
C
IgD+ CD27neg
IgD+ CD27+
overlap
CSR CD27neg
CSR CD27+
D
CB
ID2+ Ki-67+
IgD+ MZ
CB MYC+ B
CB OZ MYC+ B
E
CD5+ MZ
IgD+ CD27-
naïve CD4
CD5+ T zone
F
CD5+ κ/λ PC κ/λ overlap
G
kappa/lambda ratio
% total PC
H
Kappa/lambda ratio (plasma cells)
Kappa/lambda ratio (CD5+ LC+)
I
Significant p values (-Log10(adjusted_p_values))
-Log10(p_values)
K
Significant overlaps (multiple method)
Average cellular overlap(%)

Figure 3

Figure 3 B-cell classification and spatial distribution
A: B-cell types from five whole LNs represented as boxplots. For the boxplots specifications see Fig1. 1,443,539 cells analyzed. Average B-cells are identified by default. MZ: mantle zone; CSR: class switch recombined.
B: B-cell subtypes percentage composition of five whole lymph nodes.
C: Spatial distribution of mature B-cell types, CD27+ or CD27neg. The spatial distribution of IgD+ B-cells and CSR B-cells is shown, divided according to the CD27 expression: negative in red, positive in blue. Overlapping cells are in black. The scale represents pixels (0.45 µm/pixel).
D: The Germinal Center (GC) environment components are shown for three whole LN. Five cell types are shown: centroblasts (red), proliferating ID2+ cells (green), MYC+ B-cells (orange), outer zone GC cells (OZ) (blue). The IgD+ MZ B-cells are shown to locate the B-cell follicle (turquoise). Note the extra follicular location of ID2+ Ki-67+ and MYC+ cells. Centrocytes are not shown. An area of each image is magnified as an inset. The scale represents pixels (0.45 µm/pixel).
E: Spatial distribution of CD5+ B-cell types. The spatial distribution of CD5+ MZ and CD5+ T-zone cells for five whole LN is shown in red. IgD+ CD27- MZ B-cells (blue) and the area occupied by naïve CD4 T-cells (yellow) are shown for spatial reference. Overlapping cells are in black. The scale represents pixels (0.45 µm/pixel). The complete neighborhood and overlap chart can be seen in Figure 6.
F: Spatial relationship between CD5+ Ig light chain+ B-cells and plasma cells. The CD5+ Ig light chain kappa+ and lambda+ (red) are spatially plotted together with the kappa and lambda positive plasma cells (blue). Cell overlap is in black.
G: Kappa/lambda ratio and plasma cell frequency from BRAQUE^{global}. The two-scale graph shows the kappa/lambda plasma cell ratio for 16 LN. The first six (darker columns) are whole LN, the remaining are TMA cores, six of them duplicates. The bars (scale on the left) show the k/l ratio. The triangle (scale on the right) the percentage of PC in each sample.
H: Comparison of the kappa/lambda ratio in plasma cells and in CD5+ light chain+ (LC) B-cells from BRAQUE^{subclass}.The k/l ratio of plasma cells (blue) is compared with the same ratio for CD5+ light chain+ B-cells (orange) in six whole LN.
I, K: Neighborhood and spatial cell overlap for mature B-cells. Note two domains for GC-related B-cells (red square): a mixture of centroblasts, MYC+ and proliferating ID2+ cells and a centroblast+centrocyte proper GC. CD5+ CD27negative T1 B-cells (pink square) are neighbors, but do not have a common space allocation, although they share the space with MYC+ B-cells. CD27negative B-cells (yellow square) and CD27+ ones (violet square) co-aggregate into separate neighborhoods and occupy mutually exclusive space domains. Plasma cells, plasmablasts and light chain+ CD5+ B1 cells co-aggregate and share the same space occupancy. Color scale is on the right.

CD5+ light chain+ B-cells express high levels of kappa or lambda immunoglobulin light chain that also identifies plasma cells and plasmablasts. These cell types all occupy the medullary cords (Figure 3F, Figure S6A) (Table 1, Table S8). However, CD5+ light-chain+ B-cells have a phenotype that is suggestive of the B1 B-cell type[35], occupy a non-identical LN environment compared to CD5^{neg} plasma cells (Figure 3F) and show an independent k/l light chain ratio (Figure 3H).

Non-pathologic, incidentally discovered LN do not have a prominent follicular activation by definition and thus they may be less suited to analyze the GC reaction. In the few well-developed GC, polarization was noted (Figure 3D). Occasional centroblasts and centrocytes were found as isolated cells outside the GC, as has been described in mice LN[36] (Figure S6A).

Two additional cell types featured a spatial relationship with the GC.
ID2+ Ki-67+ and MYC+ B-cells were scattered in much of the LN interstitium, the paracortex, the follicle and entered the dark zone (DZ) and the outer zone of the GC (Figure 3D, Figure S6A). ID2+ Ki-67+ B-cells shared phenotypic traits with centroblasts and they may be part of the extra-GC wave of early B-cell activation[36].
IRF4+ PRDM1+ GC-based centrocytes were not identified, contrary to the expectation[37] perhaps due to the small size of the GCs sampled and the LN origin[32].

Extrafollicular, activated B-cells termed “immunoblasts”[38], coexpress IRF4, PRDM1 and sporadically CD30 (BRAQUE^{global}) but lack other features of plasma cells or MYC expression. This subset were found in two locations: the paracortical T-zone and the medullary cords (Table 1, Table S8) (Figure S6A).

Kappa or lambda light chain expression marks plasma cells, plasmablasts and the CD5+ light chain+ B-cells mentioned above. These cells all occupy the medullary cords (Figure 3F, Figure S6A) (Table 1, Table S8).

The ratio of circulating kappa and lambda immunoglobulin light chains in the bloodstream it has been established to be around 2:1[39]; in the tissue, wider variations of the light chain-bearing B-cell ratios have been reported[40-42]. In our samples the k/l ratio was 1.5 (SD ±1.13), falling below 1 in several whole LNs and TMA core samples (Figure 3G). We confirmed these data by segmenting and quantifying the plasma cells with traditional image analysis tools (thresholding and particle counting) and found similar values (Figure S8). Lastly, we measured the k/l ratio in 7 whole reactive LNs by in-situ light chain hybridization[43], obtaining a 1.38 ± 0.40 ratio (range 0.87- 2.17) (Figure S8C, D).

Innate immune and dendritic cells

Fourteen non-myeloid innate immune and DC types were identified by BRAQUE^{subclass}, none of which expressed CD14 or CD163. cDC1 identified in BRAQUE^{global} bore CD14 (Table S5) as other non-myeloid cells, but nested BRAQUE^{subclass} analysis revealed instead bona-fide monocytes and macrophages not previously identifiable in the DC group (Table 1, Table S8) (Figure 4A,B, Figure S6B). This was unique to DC and not seen upon re-analysis of the other cell types (not shown).

cDC1 is split into two groups: one with the canonical phenotype, cDC1A (CD74, CD141, Clec9A, LYZ, TIM3 in >70% of clusters), preferentially located in the deep paracortex and diffusely, and the other, cDC1B, with more sparse expression of the aforementioned markers (Table 1, Table S8) (Figure 4C, Figure S6B), located in the medullary cords[44].

cDC2 is also split in two main subgroups: CD207+ cDC2 (cDC2A, also known as Langerhans cells or LC) and CD207^{neg} cDC2 (cDC2B). The main differences were: expression of

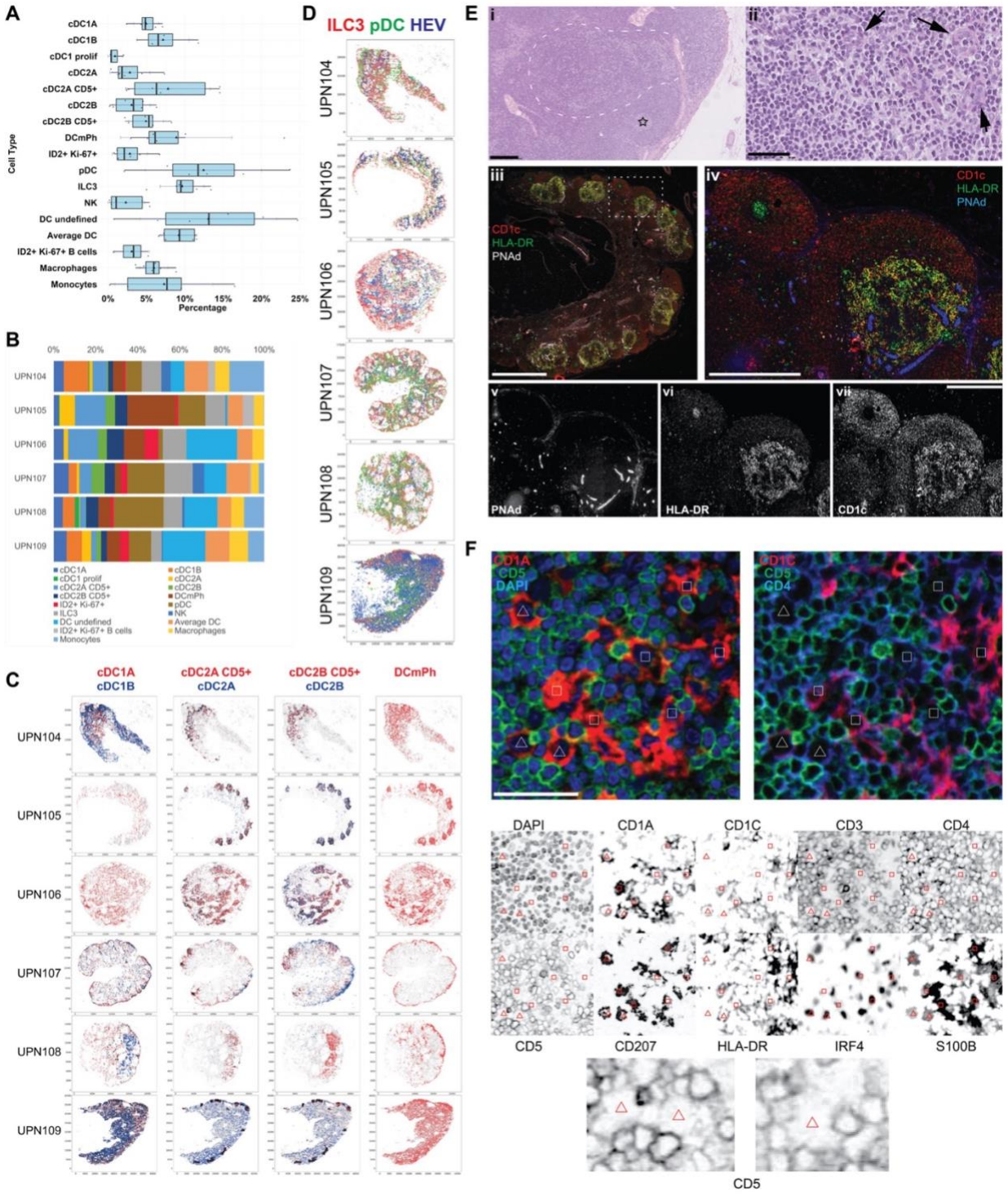
A
cDC1A
cDC1B
cDC1 prolif
cDC2A
cDC2A CD5+
cDC2B
cDC2B CD5+
DCmPh
ID2+ Ki-67+
pDC
ILC3
NK
DC undefined
Average DC
ID2+ Ki-67+ B cells
Macrophages
Monocytes
Cell Type
0%
5%
10%
15%
20%
25%
Percentage
B
0%
20%
40%
60%
80%
100%
UPN104
UPN105
UPN106
UPN107
UPN108
UPN109
cDC1A
cDC1B
cDC1 prolif
cDC2A
cDC2A CD5+
cDC2B
cDC2B CD5+
DCmPh
ID2+ Ki-67+
pDC
ILC3
NK
DC undefined
Average DC
ID2+ Ki-67+ B cells
Macrophages
Monocytes
C
cDC1A
cDC1B
cDC2A CD5+
cDC2A
cDC2B CD5+
cDC2B
DCmPh
UPN104
UPN105
UPN106
UPN107
UPN108
UPN109
D
ILC3 pDC HEV
UPN104
UPN105
UPN106
UPN107
UPN108
UPN109
E
i
ii
iii
CD1c
HLA-DR
PNAd
iv
CD1c
HLA-DR
PNAd
v
PNAd
vi
HLA-DR
vii
CD1c
F
CD1A
CD5
DAPI
CD1C
CD5
CD4
DAPI
CD1A
CD1C
CD3
CD4
CD5
CD207
HLA-DR
IRF4
S100B
CD5

Figure 4
Dendritic and innate immune cell classification and spatial distribution
A: Dendritic cell types from six whole LNs represented as boxplots. For the boxplots specifications see Fig1. Average DC are identified by default. 573,179 cells analyzed. Abbreviations: cDC: conventional DC; DC mPh: DC with mixed phenotype; pDC: plasmacytoid DC; ILC3: innate lymphoid cells type 3; NK: natural killer cells. ID2+ Ki-67+ B-cells. macrophages and monocytes were misclassified as DC in the global analysis, but re-classified after BRAQUE^{subclass}.
B: DC subtypes percentage composition of six whole lymph nodes.
C: Seven DC subtypes are plotted, six of them as contrasting color-coded in pairs, spatially plotted. Cell overlap is in black.
D: Spatial distribution of ILC3 and pDC. ILC3 (red), pDC (green) and HEV (blue) are spatially plotted on six whole LN. The scale represents pixels (0.45 µm/pixel).
E: Paracortical aggregation of cDC2 (Fairy Circles, FC). **i:** Low power H&E stain (UPN104). The dotted outline highlights a paler area in the paracortex. A star labels a small GC surrounded by a MZ. Scale bar: 250µm. **ii:** a high magnification of the dotted area in **i** shows a polymorphic cell population composed of small lymphocytes, larger blasts, larger cells with a typical indented nucleus and ample clear cytoplasm and some HEV (arrows). Scale bar: 50 µm. **iii:** low power image of LN stained in immunofluorescence for CD1c (red), HLA-DR (green) and PNAd (white). Scale bar: 250 µm. **iv:** the dotted rectangular area in **iii** is magnified. A FC in the lower right is composed of cells with a dendritic appearance and a variegation of CD1c (red) and HLA-DR (green) double expression (yellow). On the upper left, a brightly green (DR+) small GC is surrounded by a red CD1c+ follicular MZ. PNAd+ HEV (blue) are surrounding and entering the FC. Scale bar: 500 µm. **v, vi, vii:** the individual immunofluorescence components of figure **iii** and **iv** are shown individually as a grayscale. Scale bar: 500 µm.
F: RGB and grayscale composite of a single cDC2-containing area. IF images for DAPI, CD5, CD1A, CD1c and CD4 are composed as RGB color images (top half). The figure bottom half contains inverted grayscale IF images of the same area, stained for 10 relevant antigens.The polygons are reproduced in identical locations across all the images and identify cDC2. Three CD5-stained cells centered on the triangles are magnified. Scale bar 50 µm.

Langerin/CD207 and CD1a for cDC2A, and a CD4+ CD86+ prevalent phenotype and a predominant location in nodular paracortical aggregates, close to PNA+ HEV (Figure 4E) for cDC2B.
Neither group could be defined by HLA-DR or CD11c differential expression, however only cDC2A were CD1A+, a phenotype described for resident cDC2[45].
cDC2A and cDC2B were themselves split into CD5+ and CD5^{neg} subsets, as previously shown in blood[46, 47]. Both CD5^{neg} cDC2 subsets express IRF4, PU1 and BCL6, however their spatial localization was superimposable to the CD5+ cDC2s (Figure 4C) (Figure S6B). Conventional image rendering could not highlight membrane CD5 staining on cDC2, as previously shown[48](Figure 4F).

Cells with a mixed cDC1 and cDC2 phenotype, DC_{mPh}[45, 49], had CD86 as the most prevalent marker, a nondescript tissue distribution, did not self-aggregate but were neighbors of cDC2B, S100B+ activated Tregs and putative transitional B-cells (CD5+ T-zone cells) in the paracortex (Figure 4C).

We identified proliferating ID2+ cells lacking T, B or the ILC3-defining marker RORC. The recently published Ki-67+ cDC-ILC3 subpopulation[50] may therefore not reside in this fraction, but rather in the proliferating cDC1 fraction. Up to 50% of clusters express AXL, suggesting that tissue-based equivalent of proliferating ASDC [51] are contained in this group.

Plasmacytoid dendritic cells feature a very consistent homogeneous phenotype (CD303, TCF4) and a signature of IFN signaling (MX1) in >70% of clusters, as noticed previously[47] (Table 1, Table S8) (Figure 4D, Figure S6B). GZMB was not detected, as expected in quiescent pDC[52]. pDC aggregates, thought to be typical of this cell type[53], were detected in only 3/6 LN and in a minority of clusters.

ILC3s are described here in situ for the first time in LN; besides RORc, a defining but not entirely unique marker[50, 54], ILC3s expresses PU1 and a heterogeneous array of other DC-related cell markers (AXL, CD11c, CD74, TIM3) in >50% of clusters (Table 1, Table S8). These cells are found in the superficial cortex, next to HEV, as previously noted[55] (Figure 4D) (Figure S6B) and also dispersed in the outer T-cell zone, in the medulla and occasionally in the subcapsular sinus.

A single cell type corresponding to NK cells was identified and the phenotype was consistent with the consensus: CD16+ CD56+ and others[56]. NK cells were one of the smallest subsets and were often aggregated, close to macrophages (Table 1) (Figure 5C) (Figure S6B).

Myelomonocytic cells

BRAQUE^{subclass} analysis yielded 15 myelomonocytic cell types (Figure 5A, B) (Figure S9A), each one with an unique spatial distribution.

Classical monocytes were diffusely scattered throughout the medullary cords and the interfollicular interstitium (Figure S8A) with a LYZ+ PU1+ CD16^{neg} predominant phenotype (Table 1). Neutrophils shared LYZ and PU1 positivity, and in addition were CD10+, CD16+ and CD86+.

CD16 was expressed on three types of myelomonocytic cells: alternative monocytes[57], CD16+ macrophages and a subpopulation of Lyve1 perivascular macrophages, all residing within endothelium-lined spaces[57, 58].

Lyve1+ CD16^{neg} perivascular macrophages shared a similar phenotype and location as the CD16+ counterparts.

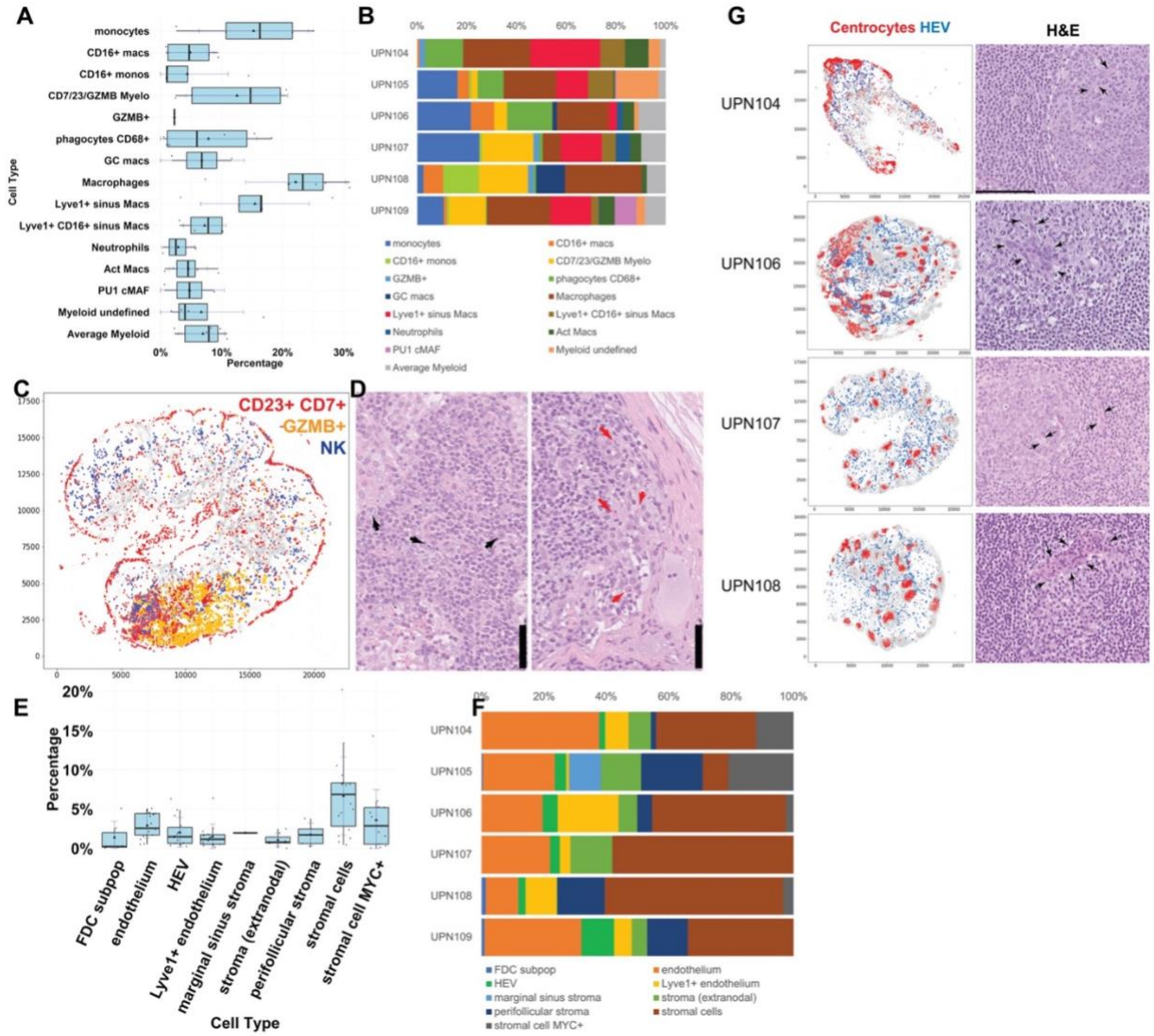

Figure 5
Myeloid and stromal cell classification and spatial distribution
A: Myeloid cell types from six whole LN, shown as boxplots. For the boxplots specifications see Fig1. Average Myeloid cells are identified by default. 588,821 myeloid cells analyzed. Macs: macrophages; Act Macs: activated macrophages; PU1 cMAF: macrophages identified by high PU1 and cMAF.
B: Myeloid cell subtypes percentage composition of six whole lymph nodes.
C: The spatial distribution of CD23+ CD7+ GZMB+, GZMB+ and NK cells is shown on the outline of UPN107.
D: High magnification of an H&E detail of UPN107 (left) shows haemorragic effusion, prominence of HEV and scattered large blasts (black arrows). Another H&E detail (right) shows a marginal sinus containing scattered eosinophils (red arrows). Scale bar = 50 µm
E: Stromal cell types from six whole LN shown as frequency ±SD. The numbers next to the bars are the number of informative cases.
F: Stromal subtypes percentage composition of six whole lymph nodes represented as boxplots.
G: Spatial distribution of HEV (blue dots) and centrocytes (red dots) in four whole LN (left panel). Scales are pixels (0.45 µm/pixel). An H&E magnified representative field is shown in the right panel. The dotted white line highlights a germinal center, the arrows point to HEV. Scale bar 100 µm.

CD11c, HLA-DR and the macrophage markers CD163 and CD68 epitomize the phenotype of two major groups of macrophages: macrophages and phagocytes, respectively[59].
Macrophages, the largest myelomonocytic cell type, had a preferential distribution in the medullary cords (Figure S9A), were more consistently represented in the LN examined and the phenotype was dominated by markers conventionally regarded as myelomonocyte-specific (CD14, CD31, CD68, CD163, TIM3, AXL) (Table 1).
Two types of cells had a consistent, highly expressed CD68+ phenotype: GC macrophages and interstitial phagocytes, often expressing CD86, MYC, PDL1, HLA-DR (Table 1) (Figure S9A).

BRAQUE found additional four cell types not previously described.
Two subsets had GZMB expression in common, one also displayed CD7, CD23 and IDO (Table 1), both were located in focal parenchymal aggregates (Figure 5C) (Figure S9A), together with NK cells and where morphological signs of cell activation were noticeable (Figure 5D). The lineage affiliation of these two subsets is unknown.
Of the two other types, one (Act Macs) expressed MYC, TIM3 and other non-lineage specific biomarkers, and the other had a CD163, cMAF, PU1 phenotype (Figure S9A).

Non-hematopoietic stromal cells identified in normal LN
Although non-hematopoietic stromal cells were not targeted specifically in the analysis, about a quarter of the markers evaluated were shared between lymphomyeloid and stromal cells (Figure S1), a few were stroma-restricted, allowing a cell classification for the latter. CD248/Endosialin and vWF, both restricted to non-hematopoietic cells (megakaryocytes are absent from LN), only labelled stromal and endothelial cells (Table 1 and Table S5), providing proof of the single-cell specificity of both the segmentation and the BRAQUE pipeline.

Follicular dendritic cells (FDC), endothelial cells and fibroblasts, these latter named “stromal cells” because of absence of classifying markers (named NESC, non-endothelial stromal cells by Abe et al.[9]) were subclassified into ten cell types (Table 1) (Figure 5E, F)(Figure S9B).

Endothelial cells were classified according to the expression of CD31, shared with myeloid cells, and lineage-associated markers such as Lyve1 (this one restricted to lymphatic and sinus-lining endothelium), vWF, CD34, TCF4 and MYC. The last three were also found on non-endothelial stromal cells.

Lyve1^{neg} capillary endothelium could be subdivided in two groups, high endothelial venules (HEV) and conventional endothelial cells because of tissue distribution and subtle phenotypic details. HEV were allocated in the paracortex, had shorter, broader branching, and expressed MYC. PNAd was invariably one of the first three ranking significant markers (Table 1). Of note, centrocytes were found adjacent to HEV (Figure 5G)

The coexpression of SOX9 and TCF4, together with CD248, AXL and AID defines LN fibroblasts, some MYC+, diffuse through the LN parenchyma or lining defined structural units (capsule, medullary sinuses, vasculature). The extralymphoid expression of AID has been documented in primary fibroblasts[60], albeit at 1/10th of the levels in B-cell lines. Coexpression of TCF4 and SOX9 message has been reported in fibroblasts, TCF4 only in endothelial cells (BioGps, http://biogps.org last accessed Feb 26, 2024)[61].

Some LNs contained a peri-follicular population of stromal cells with peculiar markers (CD11c, CD141, TIM3).

Extranodal stromal cells had a different phenotype, characterized by AXL, BCL6, cMAF and Zeb1.

Neighborhoods of the normal human LN

We computed the statistical significance of the neighborhoods with two different approaches: firstly with a fisher test, significant when the neighboring cells were particularly enriched in a given cell type, and then with a method based on cellular “overlap”, to better quantify stronger / weaker cellular spatial relations (Figure 6).
Together with statistical tests, we wanted to evaluate a further metric, the median distance to the nearest cell of and from each specific population (Figure 6, Table S9 and Table S10), which may provide further information.
We could confirm known neighborhood relationships such as CD4 T-cell subsets (S100B+ effectors and activated Tregs) with cDC2[62-64], centrocytes and MZ B-cells with DC[65, 66], plasma cells with macrophages[67], the heteroaggregation of light chain positive plasma cells, and the self-aggregation of several, but not every cell type[68].

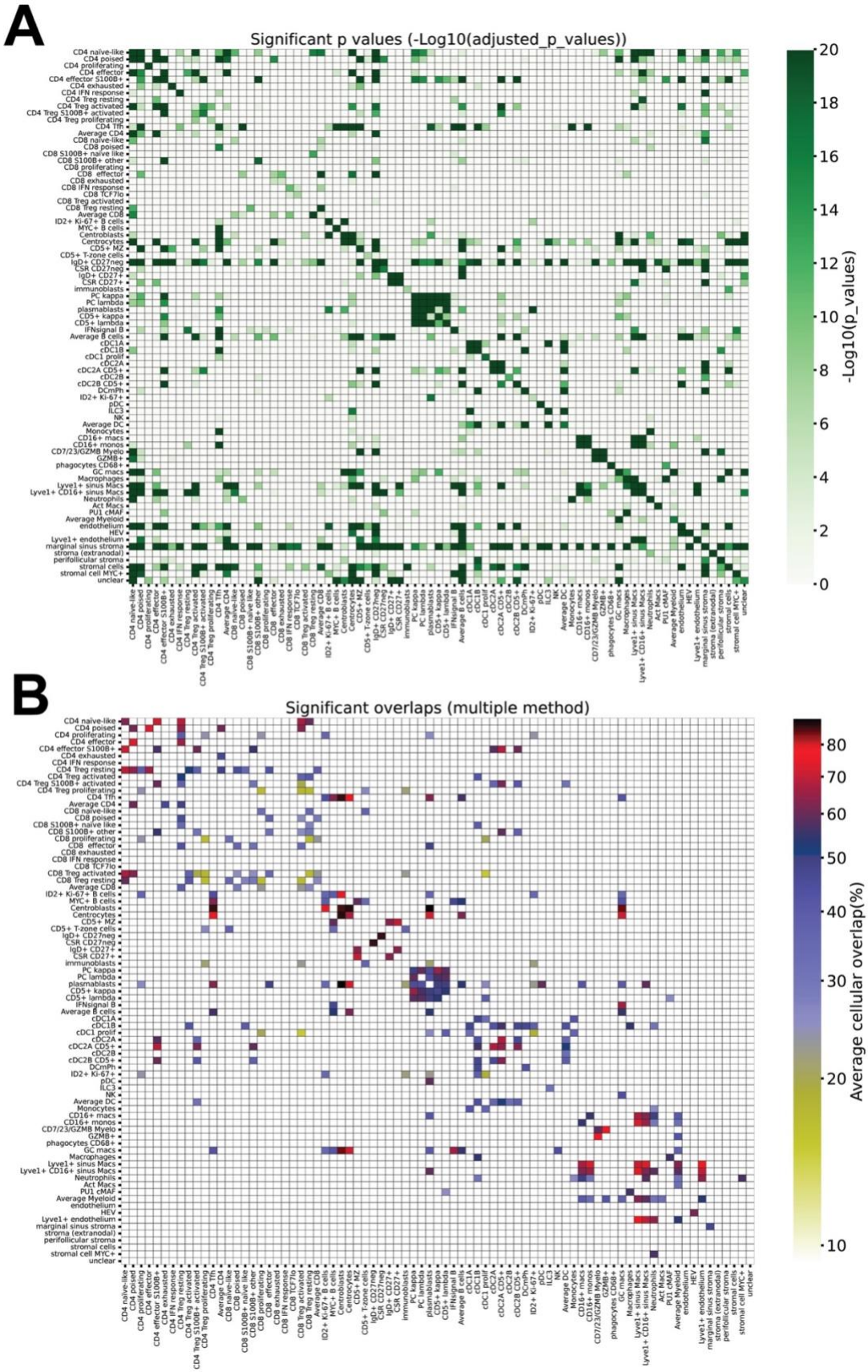
A
Significant p values (-Log10(adjusted_p_values))
-Log10(p_values)
B
Significant overlaps (multiple method)
Average cellular overlap(%)

Figure 6
Neighborhood and cell type overlap
A: Neighborhood relationship between cell types. The figure contains all statistical significance values for each cell type (rows) versus the others (columns). Only the values equal or smaller than p 8.094544277157197e-06 (approx. 0.0000081) are shown. Color scale at the right.
B: Overlap for each cell type (rows) versus the others (columns). Only the values equal or smaller than p 8.094544277157197e-06 (approx. 0.0000081) are shown. Color scale at the right.

Other described neighborhoods were not confirmed: cDC1 and CD8[69], cDC1 and HEV[44], macrophages and fibroblasts[70], ILC3 and endothelium or plasma cells[71]. Several CD4 and some CD8 T-cell types bound to endothelium, but none to HEV[72].
The reason for this may be a combination of LN selection, the strict significance criteria and/or the insufficient number of samples for a specific immune challenge.

Unanticipated novel neighborhoods were found.
A previously undescribed TCF7^{lo} CD8 T-cells co-localized with CD8 showing IFN response (Figure 2D).
IgD+ CD27^{neg} MZ B-cells are neighbors of plasma cells (Figure 3I, Figure S7B).
Centrocytes interacted with HEV and endothelium, the normal counterpart of the morphologic detail (penetration of GC by vessels) seen in unicentric hyaline-vascular variant of Castleman's disease[73] (Figure 5G)(Table 1).

The landscape of the normal human LN

By computing the overlap of each cell type versus each other, we draw a detailed landscape of the LN immune architecture (Figure 2E, 2F, Figure 3I, 3K, Figure 6, Figure S10). In general, each cell type overlaps with 4.2 ± 3.3 (range 0 - 18) of the other cell types, pointing to a very specific landscape occupancy. This is very informative of both the shared and the mutually exclusive spaces.
An analysis of the statistically significant distribution of the cell types in the LN zones (Figure 7) reveals a few specific positive locations and several specific avoidances, not entirely unexpected for *a*) motile cells *b*) in LNs whose immune status is heterogeneous.
Non-naïve CD4 TCF7^{hi} or TCF7^{average} T-cells occupy the LN paracortex, a landscape in which no other cell types were preferentially located, except cDC1 and cDC2. Exhausted CD4 spread to the medullary cords and activation spots and did not overlap with other cell types (Figure 2D).
CD4 T_{fh} cells, centroblast, centrocytes and the GC-related B-cell subsets occupy a GC environment, also shared with plasmablasts and GC macrophages.

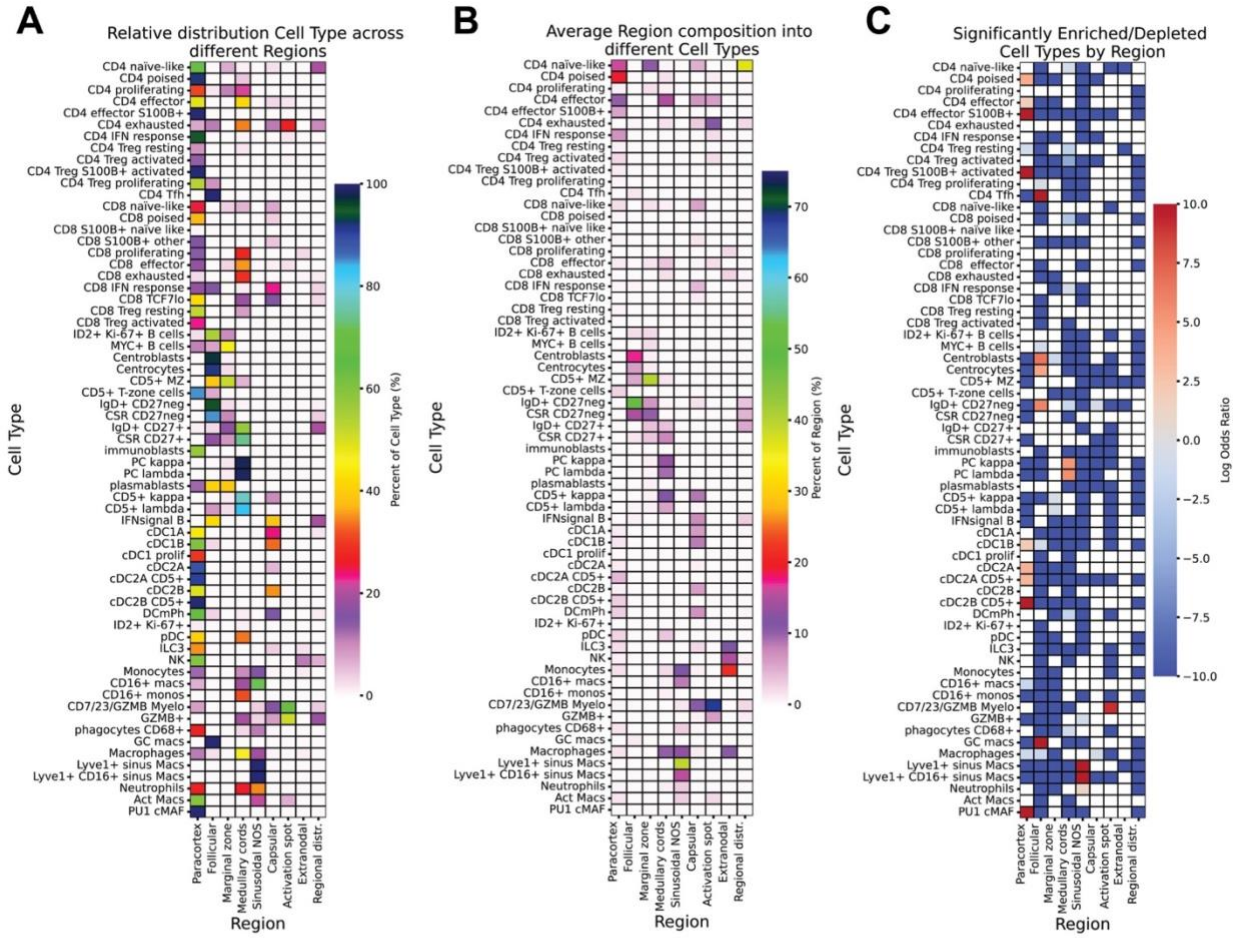

Figure 7

Distribution and statistical significance of cell types across the LN regions.
A: Relative distribution of each cell type across different regions. Each horizontal line sums to 100%. Scale on the right.
B: Average region composition in terms of cell types. Each vertical column sums up to 100%. Scale on the right.
C: Significantly enriched/depleted cell types per region, showing average log odds ratios from Bonferroni corrected fisher tests. Scale on the right.
Data for UPN104-108.

The analysis of mature B-cell overlap revealed five non-overlapping spaces (Figure 3I, K).

The first space comprises a dual aspect: GC-based centroblasts and centrocytes, but in addition largely extrafollicular ID2+ Ki-67+ and MYC+ cells admixed to centroblasts, a structure which may consist in the outer zone (Figure 3D, K)[74].

The second space contains CD5+ CD27^{neg} putative T1 B-cells, but also MYC+ B-cells (Figure 3I, K). A “marginal zone” definition may fit the distribution of CD5+ MZ B-cells.

The third hosts CD27^{neg} IgD+ or negative B-cells and corresponds to the MZ.

The fourth space is occupied by CD27+ MBC and may represent a newly described memory B-cell zone (MBZ). This zone was not included among the established LN zones, thus will not appear in Figure 7 and Table S12.

The last corresponds to plasma cells, plasmablasts and the CD5+ light chain+ B-cells in the medullary cords.

cDC2A and CD5+ cDC2B share a space with each other, S100B+ CD4 effectors, S100B+ $CD8_{others}$ and CD4 T_{reg}s.
These cDC2 cells in real space revealed circular paracortical structures with an empty center, reminiscent of the nodules described before[75] (Figure 4E). We expanded the morphological analysis of these structures to 12 whole LN sections and 99 cases of various non-neoplastic LN pathology or morphologic variations of normalcy, by using robust cDC2 markers (CD1c and HLA-DR) and reviewing at low power the IF images (Table S13). Because of the morphological reminiscence of these circles with another biological phenomenon (https://en.wikipedia.org/wiki/Fairy_ring), we named these “Fairy Circles” (or Focal Clusters; FC) .
Well organized FC were visible in 92% of 12 whole sections and 56% of 16 2mm TMA cores from “normal” LN. FC were absent from 75% of pathological TMA cores and from all the pathological whole sections images (Table S13). Individual cells from these latter samples were not analyzed, therefore we cannot comment whether the disappearance of FC is mirrored by qualitative/quantitative changes in cDC2.
As described previously[75, 76], PNAd+ High Endothelial Venules (HEV) were found close to or encroaching the FC (Figure 4E and Figure S13).

The perivascular space is occupied by CD16+, Lyve1+ perivascular macrophages, the latter sharing the space with Lyve1+ endothelium.
GZMB+ cells tend to occupy a space by themselves, shared with PU1+ Macs.

DISCUSSION

We have used a 78 antibody-strong panel, an epitope- and tissue-saving technique, MILAN[12, 77], and a recently developed novel bioinformatic pipeline, BRAQUE[10], to classify the cells constituting the human LN into 77 cell types according to known phenotypes and published and unpublished spatial landmarks. The integration of the phenotype and the tissue distribution of the individual clusters from BRAQUE has been fundamental for an extended cell identification.

The classification obtained features a combination of surface, cytoplasmic and nuclear proteins detected at high sensitivity[78], thus providing an invaluable proteomic granular reference dataset for molecular or multi omic data integration.

This is the most detailed classification of the whole LN performed in situ up to date and represents LN “normalcy” by size, histopathology and clinicopathologic standards[79]. Size has been the only parameter useful to classify a LN as “normal”[79, 80]; we can now add preserved immune structures (FC) or phenotypic traits (absence of GZMB from pDC) as hallmarks of normalcy.

As shown in Table 1, the phenotypes and the cell types we describe have been extensively cross-validated in years of immunology research, quoted throughout the text and, more recently, by scRNAseq studies of the SLO within the HCA initiative[81].
Interestingly enough, this latter comprehensive study, which orthogonally validates the vast majority of our cell types, fails to identify IFN signal in T cells, transitional and B1 B cells, alternative macrophages and other cell types probably because of a weak correspondence between RNA and proteins[82, 83] and more favorable representation of biology by proteins, compared to RNAs[82]. The fact that transcriptomics may be less suited for the classification of lymphoid tissue is confirmed by recent studies[24, 84].
In the Caron study[24], a 265 antibody CITEseq panel aimed at surface markers shares with us 44 antibodies only, and lacks transcription factors and intracellular markers: it fails to identify in peripheral blood several lymphoid cell types we describe in the LN. While transcription factors alone do not suffice to classify cells (our data) other factors may be the cause besides the lack of intracellular markers: an elaborate signal thresholding algorithm (vs no gating in BRAQUE), and the focus on peripheral blood (vs LN).

We provide spatial relationship data and anatomical allocation for numerous cell types for which, in the authors’ knowledge, only transcriptomic studies on cell suspensions or some single staining information were available. This is the case for putative B1 or T1 cells, memory B-cells, CD5+ cDC2 and several subtypes of T-cells with function-associated phenotypes. In addition, we suggest a dedicated nodal site for memory B-cells, which we named memory B-cell zone (MBZ).
A nodal equivalent to the splenic marginal zone has been described in the subcapsular and medullary LN sinus in mice[85] and in parasite-infected humans[86]; these reports hint at a

subcapsular sinus location for MBC in humans. We found clusters with such spatial distribution in 2 LNs only.
Between 1986 and 2001 hematopathologists [87-89] have described in non-pathological LN an indistinct and variable collection of cells with clear cytoplasm (monocytoid) located outside the mantle zone and bearing phenotypic features similar to the splenic marginal zone. This may be an earlier description of a nodal location for MBC, distinct from the MZ, based however on a very limited phenotype.
DN B cells (IgD^{neg} $CD27^{neg}$) have elicited considerable attention lately: they have been linked to autoimmune disorder, chronic infections (HIV, malaria) and cancer[30, 90] and thought to belong to an extrafollicular antigen response. To co-locate DN B cells with naïve MZ B cells in the follicle, apart from MBZ cells, is a novel finding.
The elusive CD5+ B1-like human B cell population is resolved in spatially and phenotypically distinct cell types, expressing TCF7, a finding very recently confirmed in blood and peritoneal effusions, but not in SLOs[91].

A combination of immunophenotyping, high-dimensional analysis and traditional histopathology has detailed circular gathering of cDC2 reminiscent of the “fairy circles”.
These novel descriptions should prompt additional research to elucidate the composition, the stromal underlying and the dynamic of these novel zones.

A hyperplexed targeted Ab-based in situ proteomic investigation inherently relies on Ab specificity[92] and sensitivity, posing novel challenges[78]. The profile of each cell type in this study is obtained by listing the most frequently reported markers among the numerous clusters belonging to that type, not the most highly expressed. In BRAQUE these latter correspond to higher “effect size”[10, 78] and are reported in a separate column in Table 1. Keeping that in mind, we faithfully reproduced established phenotypes, thanks to the redundancy of the panel used, but also listed are markers which have been reported only in experimental condition or in cell suspensions and never in FFPE tissue.
That is the case for CD23 in T-cells and myelomonocytic cells[93, 94], CD7 on myeloid cells[95], TCF4 on endothelium[96], AID on fibroblasts[60] and CD5 on B cells and DC.

We report coexpression of markers (e.g. BCL6 and PRDM1) initially described to be mutually exclusive[20, 37, 97], but later revised in some cell types[98, 99]. The protein half-life[82, 83, 100], the mutually inverse gradients of expression[100-102] and the aggregation of multiple clusters in a

single cell type may substantiate the results obtained by BRAQUE. Lastly, BRAQUE scores as statistically relevant values not appreciable by signal thresholding and/or visual assessment[78].

Canonical markers are conspicuously missing in BRAQUE^{subclass}: CD3, CD5, CD7 and BCL2 in T-cells, IRF4 on MZ B cells[37], CD30 on B-cells[103], etc. This is because BRAQUE lists the statistically significant markers which make each cluster unique and not the antigens broadly expressed in the target population, thus not making the statistical threshold[10, 78]. Therefore, the phenotypes defining cell types in this work need to be integrated with canonical markers for tasks such as single cell manipulation.

LIMITATIONS OF THE STUDY

The neighborhood analysis of this study represents a “minimalist” view of the interactions, given the very strict requirements to produce a significant score (10 AND 20µm, significant in all LN examined); tissues harmonized for a specific immune response may disclose additional meaningful interactions.

For some phenotypes a definite explanation is not available and deserves further study. This is the case e.g. for CD23, which ranks among the five top-ranking markers in FDC and CD27neg CSR, where it is expected, but is listed on CD27+ MBC, where it should not be according to previously published data[104]. The possible reasons may be Ab specificity, the inner working of the dimensionality reduction algorithm or the post-transcriptional regulation of CD23, which is particularly complex[105] in tissues.

One may also consider that secreted/soluble proteins do diffuse in tissues (e.g. GZMB[106], vWF[107]) and are detected by BRAQUE, independently from the segmentation inaccuracies.

Other limitations of this study encompass the failure to identify cell types minimally represented in quiescent LN such as γδ T-cells, double negative T-cells, RORγτ+ T-cells, AXL+ DC[108] and NK cell subsets[109]. The reasons may be the insufficiently diversified markers panel, the unappreciated broader distribution of markers described to be dichotomic in expression, the limitation of the segmentation protocol, the inherited problems of fixed and embedded material, unknown limitations of BRAQUE or a combination of all of that.

This study will help to consolidate an holistic view of an “average” human LN landscape, if ever such a definition may apply to the immune system in general, allowing the comparison with immune perturbations, particularly the ones not driven by clonal expansions, but fixed in timing and in stimulus drivers.

MATERIALS AND METHODS

EXPERIMENTAL DESIGN

Human specimens

Lymph node excisional biopsies and clinical notes were extracted from the laboratory information systems of the collaborating centers by the Authors with clinical privileges and anonymized. The inclusion selection criteria were: *i*) absence of pathology, inflammatory, autoimmune or neoplastic, *ii*) non-specific nodal changes in the histology description (e.g. paracortical or follicular hyperplasia, sinus histiocytosis), *iii*) any anatomical location, *iv*) uninvolved sentinel LN from breast or lower GU tract, or incidental finding, *v*) small size; the chosen samples measured an average=0.98 cm, SD+/- 0.35 cm for the shorter axis, n=19; for six whole LNs: average=0.87 cm ± 0.28, range: 0.62-1.41 for the shorter axis. Note that the size reference values for normal LN does not exceed 1 cm. for the shorter axis[79, 80], irrespectively of the organ site[80].
A progressive UPN (Unique Patient Number) was assigned to each patient. Paraffin blocks and sections to be analyzed were selected by a Pathologist after a review of the Hematoxylin and Eosin (H&E) stain. Only archival formalin-fixed, paraffin embedded material (FFPE) was used. The clinicopathologic and biometric data of the cases comprising the dataset are listed in Table S1.
None of the LN contained particulate material[110].
The study has been approved by the Institutional Review Board Comitato Etico Brianza, N. 3204, “High-dimensional single cell classification of pathology (HDSSCP)”, October 2019. Consent was obtained from patients who could be contacted or waived according to article 89 of the EU general data protection regulation 2016/679 (GDPR) and decree N. 515, 12/19/2018 of the Italian Privacy Authority.

METHOD DETAILS

Tissue Microarray (TMA) preparation

Tissue microarrays (TMA) were prepared as previously published on a Tissue Microarrayer Galileo model TMA CK4600 (RRID:SCR_024393) (Integrated System Engineering S.r.l., Milan, Italy). Cores of 2 mm were used, from selected areas annotated by a Pathologist. Duplicate cores were placed in two separate TMA recipient blocks.

Histology repository

Virtual images of H&E stained sections, serial to immunostained ones, were deposited in a NDPIserve (RRID:SCR_017105) (Hamamatsu Photonics), available at: https://tiny.cc/LNproject

Anatomical terms and definitions

The anatomical boundaries or the LN were defined as previously described[1, 111]. The terms used throughout the manuscript are detailed in Table S14. A UBERON terminology (https://evs.nci.nih.gov/ftp1/UBERON/About.html; last consulted on September 4th 2024)[112] was added when suitable (Table 1, Table S1 and S14).

Antigen retrieval

Antigen retrieval (AR) was performed once placing the dewaxed, rehydrated sections[12] in a 800 ml glass container filled with the retrieval solutions (EDTA pH 8; 1 mM EDTA in 10 mM Tris-buffer pH 8, Merck Life Science S.r.l.,Milano, Italy; cat. T9285)), irradiated in a household microwave oven at full speed for 8 min, followed by intermittent electromagnetic radiation to maintain constant boiling for 30 min, and cooling the sections to about 50° C before use.

Antibody validation and staining

Antibodies were validated according to published protocols[92, 113]. A list of antibodies is reported in Table S2, which also contains the cycle round number and the fluorochrome for the secondary antibody.
Representative low-power and high-magnification images of a whole LN staining is provided in Figure S1A, B.
The full panel consisted of 97 immunostains (+ EBER and autofluorescence). 20 antibodies who produced inconsistent staining were excluded from the analysis (Table S6). Viral biomarkers (EBV, HHV8) were not analyzed in this dataset.
As an additional tool to explore expected relationships among variables (antibodies), a correlation matrix was constructed for sample UPN 107 .csv as a reference.
The R function “corplot” (order = AOE) was used for the representation. It provides a coloured table which represents the positive or negative correlation of one single marker versus the others. The order of markers is established according to the AOE parameter (the angular order of the eigenvectors) which is supposed to group markers with the same behavior.
A coloured side bar (representing the IF channel of acquisition of each marker, green= FITC, yellow= TRITC, RED= Cy5, BLUE= BV480) with a number (the staining round) is reported next to the biomarker (Figure S1C).
The preferential cell type distribution of all antibodies is reported in Supplementary Figure S1D.

MILAN Immunofluorescence

Multiple immunofluorescent (IF) labeling was previously described in detail with the MILAN (Multiple Iterative Labeling by Antibody Neodeposition) method[12, 77].
Briefly, the sections were incubated overnight with optimally diluted primary antibodies in species or isotype mismatched combinations (e.g. rabbit + mouse, mouse IgG1 + mouse IgG2a, etc.), washed and counterstained with specific distinct fluorochrome-tagged secondary antibodies[12]. The list of primary and secondary antibodies is in Table S2. The slides, counterstained with DAPI and mounted, were scanned on an S60 Hamamatsu scanner (Nikon, Campi Bisenzio, FI, Italy) (RRID:SCR_022537) at 20x magnification (0.45 µm/pixel) 8 bit. The filter setup for six color acquisition (DAPI, BV480, FITC, TRITC, Cy5) plus autofluorescence (AF) was as published[114]. After a successful image acquisition, the sections were stripped according to the MILAN method[77] and stained with another round.
Five slides (either whole sections of TMA) were processed simultaneously as described[77] to minimize intersample variations. Staining variability for the same Ab set after ~30 cycles was less than 15% and no method-dependent cell loss was noticed (see Supplementary Fig. 1 in Manzoni et al.[115]).

Preparation of immunofluorescent images for single cell analysis.

A pipeline, A.M.I.C.O.[116, 117], was adapted and used to register all the images belonging to a case or a TMA and rename each image with the biomarker name, according to a signpost-containing file name and fluorescence channel saved at acquisition.
After the stainings were acquired, digital slide images (.ndpi) were imported as uncompressed .tiff with ImageJ (ImageJ, RRID:SCR_003070). Tissue autofluorescence (AF) was subtracted when appropriate as published[12]. In order to remove the contribution of circulating polyclonal immunoglobulins (versus the monoclonal membrane-bound or cytoplasmic Ig)[118], after AF subtraction, images for lambda light chains were subtracted from kappa light chains images, after equalizing the intensity of the former; the same was done for kappa light chains. The resulting image (kappa sine lambda and lambda sine kappa) were used for the analysis.
No other digital image modification was applied.

Validation of the analytical pipeline

Cell segmentation

A DAPI nuclear stain-based, Matlab-based segmentation algorithm, CyBorgh[10], was applied. CyBorgh algorithm output is a .csv file obtained by applying an expanded-nuclear mask to all registered images.tiff (one for each marker) belonging to a sample. In detail, for each cell, it is extracted the mean value among pixels (8 bit grayscale) related to each marker/image.
Data extracted for each single cell x image associated with spatial x and y coordinates composed the final matrix used for the analysis. Columns represent the variables (mean value per marker and spatial information), row the cells.
This algorithm was compared with Cellpose2[119] (https://www.cellpose.org/; latest access 25 december 2023) by segmenting three 2 mm. TMA LN cores (UPN26, 32, 33) with both and comparing the cluster output and composition (Figure S2A and Table S15).
The code for CyBorgh can be downloaded from doi: 10.17632/3ntbp3zdzh.1.

Artifact identification and subtraction with BRAQUE

HDBSCAN, which is part of the BRAQUE pipeline[10], identifies outliers (e.g., cells having marker profiles heavily different from everything else, and similar to nothing else within the sample) as noise points and allocates them by default as a “-1” cluster, which acts as a garbage collector, and whose numerical dimension has been calculated for each sample and reported in Table S7.
In addition, the preprocessing step by BRAQUE allows a precise identification of artifacts (focal tissue loss, scratch, tiling borders, staining focal or partial defects, etc.) as separate clusters with an unique phenotype and spatial distribution, which can be manually excluded from the analysis (Figure S2D).
The pipeline discriminate cell types which are closely commixed with others, e.g CD4 and CD8 T-cells[10], stromal cells and endothelium, sinus-lining macrophages and endothelium etc., without applying computational corrections for signal crossbleeding[120] (Figure S2B).
To test the robustness of BRAQUE in the presence of non-specific noise, we run a sample (UPN32) before and after subtracting the AF. As shown in Figure S2C, BRAQUE was moderately affected by noise. (Figure S2C and Table S16).

Antibody panel high dimensional validation

We next tested how a reduced antibody panel would affect the results. Three panels were designed (Table S6 and Figure S2E) and run on two whole LN (UPN107 and UPN108):

- 33 “non-redundant” Abs: lineage-defining Ab with minimal or nil staining across the other lineages (e.g. CD3 and CD20).
- 41 “TF and friends” Abs: all the anti-TF Ab and a selection (16) of lineage-defining Ab
- 68 “only clean” Abs: Ab chosen for high signal-to-noise ratio.

Compared to the full Ab panel, each of the reduced panels had variations in detection or representation (Table S17). The TF panel was the most affected, having the highest junk and uninterpretable results. Some cell types (Treg, plasma cells, RORC) had the most consistent results, probably because of a combination of unique highly characterizing markers and a distinct phenotype. We also found that a minimum of ~68 markers (Figure S2E and Table S6) is required for the cell classification of most hematolymphoid cells.

An analysis of the TMA cores with Seurat[121] produced a 23 cell type classification of the LN analogous to BRAQUE (Figure S3).

Sample size representativeness

A comparison of the cell type composition of whole LN sections (WSI) vs TMA cores shows that these latter are representative of the whole sections except for the smallest populations, which were under- or over-represented because of the pathologist-driven targeted sampling, notwithstanding the 2mm diameter TMA cores (Figure S4).

Iconographic rendering

Computer-generated .png files were re-colored, modified and assembled with the following softwares:
Fiji (RRID:SCR_002285) (https://imagej.net/ last accessed January 15 2024)[122]
Adobe Photoshop 25.3.1 (RRID:SCR_014199)
Adobe Illustrator 28.1 (RRID:SCR_010279)
RGB composite immunofluorescent images were imported as grayscale images into Fiji, optimized via the Brightness/contrast tool automatic function, cropped and colored as desired.

QUANTIFICATION AND STATISTICAL ANALYSIS

High dimensional analysis with BRAQUE

Data extracted from a tiled set of images after CyBorgh segmentation were processed via a bioinformatic pipeline, BRAQUE[10].
BRAQUE is a python pipeline for automated cluster enhancing, identification, and characterization. The output consists of multiple clusters, whose numerosity is defined by the size of the smallest cluster (usually not below 0.005% of the cell number or ~20 cells). Each cluster is defined by A) markers ranked by probability or possibility to identify the cluster (i.e., a robust measure of effect size comparing within cluster marker distribution with outside cluster marker distribution), B) a tissue map of the cells belonging to the cluster and C) the expression of a pre-defined set of diagnostic markers for that cluster, compared to the whole population. Each cluster is classified by an expert supervision into cell types[78]. The parameters to apply BRAQUE to the LN dataset were tuned by varying the parameters and scoring a sample. Once the results were satisfactory, BRAQUE was applied to the whole dataset (see Supplementary material @ doi: 10.17632/3ntbp3zdzh.1).

BRAQUE preprocessing

The usage of Lognormal Shrinkage showed consistent and significant improvement in terms of all the following aspects: better cell groups separation in the lower dimensional embedding, more consistent and compact individuated cell types, smaller number of unclear cells (labeled in the "noise" cluster), highly reduced number of spurious “mixed phenotypes” such as CD4+ CD8+ T cells, CD20+ T-cells etc (See Table S3, Table S15).

Gaussian Mixture Components:

Given G_i as the initial Gaussian mixture components number, and G_f as the final number of components, selected by the algorithm at convergence.
We observed that a higher number of G-i strongly helps to scatter different cell types apart, reaching a plateau in performances around 20~30.
Moreover, we wanted G_i to be higher than G_f for all markers, in order to check the algorithm had enough starting components and was not limited by input parameters (since G_i acts as an upper limit for G_f, and the algorithm can drop useless components but not add useful ones if needed).
Lastly we know that higher G_i means significantly higher computation times, and therefore we considered choosing for it the smallest value for which G_i > G_f for all available markers, resulting in 20 for all lymph nodes except for the largest one, UPN109, for which we used 28.

BRAQUE nested classification:

We decided to apply our pipeline in a hierarchical fashion, first by identifying clusters of either B-cells, CD4+ T-cells, CD8+ T-cells, Dendritic cells, Myeloid cells, or other cell types ($BRAQUE^{global}$).
The non-hematopoietic cell types (such as endothelial cells) were definitively assigned to their cluster, while for each of the other subtypes we performed the pipeline once again, apart from the preprocessing step, on a specific subset of markers (Table S6) ($BRAQUE^{subclass}$). Unclear, unassigned or noise clusters were discarded from the analysis (e.g. noise cluster cells, unclear cell types with contradictory markers, unseparated T-cells etc.)
This decision was due to how most cell types are interpreted and defined. A very specific and selective set of markers is necessary to sub-specify e.g. two B-cells or two CD4 T-cells, being the rest of the panel unnecessarily noisy and uninformative in the analysis.
In the $BRAQUE^{subclass}$ analysis, the HDBSCAN “-1’ cluster refers to an “average” cell of the cell type analyzed, not to cells of unassigned clusters, as in $BRAQUE^{global}$, which were excluded from $BRAQUE^{subclass}$ analysis.

Minimum size of cell group:

Minimum size of a cell group is a parameter which needs to be tuned for new hyperplexed images dataset and new antibody panels. In our case, reducing this number might lead to more, clearer, and smaller clusters, while raising it causes more cells to enter the "unclear" cluster. Tuning these parameters based on the number of resulting clusters led to faster and better separation of clearer cell types, and therefore we assessed it in the range of 100~300 cells, which led to 50~100 clusters for each cell subtype among B-cells, CD4 T-cells, CD8 T-cells, Dendritic cells, and Myeloid cells. The smallest cluster (10 cells) consisted of CD8 naïve T-cells, the largest (101,180 cells) of IgD+ CD27neg B-cells.

BRAQUE data output and analysis

Each cluster was evaluated by examining the following types of data:
i) the comprehensive list of markers significantly expressed with respect to the average sample distribution (via a Welch t-test),
ii) the ranking of said markers according to their decreasing effect size (so to have overexpressed markers as most characteristic ones),
iii) the expression of selected lineage-defining markers (these independently from the ranked list) and
iv) the spatial location within the tissue.
The output of the pipeline has been described before[10, 78].
Since no signal thresholding was performed, intersample pre-analytical variations (fixation, processing etc.) which may modify the tissue antigenicity, would not affect the relative ranking of cluster-defining markers across samples.
Clusters were classified according to the similarity to known phenotypic consensus profiles in published papers. Clusters with incoherent markers were classified as “junk” and discarded. Phenotypes not published before were either classified as “undefined” or grouped in homogeneous new phenotypes. Classified clusters were grouped into individual cell types. This process was performed independently by two investigators (GC and GEM) and harmonized.
In order to build a comprehensive list of markers for each cell type, two type of data were extracted from the ranked list of markers of each cluster (Table 1, Table S18, Table S19): the list of markers present in 70-100%, 50-69% and 30-49% of all clusters belonging to a given cell type and the list of the markers ranked 1st to 5th in that cell type. To compute this latter, we calculated the median value of the position of a given marker in each ranked list for the clusters belonging to that cell type and listed the makers ranking from 1st to 5th place.
The two types of data provide independent information: the first lists the markers identifying a given cell type, independently of the signal-to-noise ratio, the ranking or the statistically significant effect size. The second reflects the effect size and, combined with the first, which marker best applies to flow-cytometry or visual immunostains for cell detection in tissue; it may be used as a proxy for signal brightness, but may represent only a fraction of the clusters of that cell type.
Further analysis of how BRAQUE compares with previous pipelines has been reported[78].

Post-classification data analysis

Neighborhood analysis

We computed the statistical significance of the neighborhoods with two different approaches: first with a fisher test and then with a newly devised method based on cellular “overlap”.
The reason behind this double approach resides in the fact that the former represents a classical/dichotomic approach (near/far, significant variation in odds ratios), while the second highlights a rather continuous measure (how near? More than randomly expected?), giving different importance to neighboring cells based on their spatial closeness (Figure 6).
The overlap test briefly consists of assigning each cell an interaction radius, and then compute the observed and expected amount of pixels (i.e, infinitesimal elements of area) covered by both interaction radii of neighboring cells for different populations (or even same for same population overlap). The pixel-hitting procedure is the equivalent of a Bernoullian process, with success probability given by the ratio between cell interaction area and whole lymph node area. Therefore the overlap is computed using Binomial cumulative density functions.
To increase statistical robustness of outcomes, the analysis was repeated using 2 different distance thresholds to define neighbors, specifically 10μm and 20μm[123].

In other words, neighboring effects were considered significant only if the analysis using 10µm (22 pixels) threshold and the analysis using 20µm (44 pixels) threshold were both significant for the given neighboring effect over all available samples independently. Both tests were corrected for multiple tests with Bonferroni correction.

Considering cell population A and B, this translates into taking the maximum of the p-values measured across all samples with both populations, and consider it significant only if the maximum p-value was below the Bonferroni corrected significance threshold.
These measures (max p value, together with Bonferroni correction, considering 6 lymph nodes each with 2 different thresholds) allowed for maximal protection against false positives, meaning that all the reported outcomes had been consistent over all samples and with highly significant performances.
Together with statistical tests, we wanted to evaluate a further metric, the median distance to the nearest cell of and from each specific population (Figure 6, Figure S10, S11 and S12), in order to provide further information.

Overlap

We start by defining an interaction radius for each cell, by drawing this imaginary interaction circle, centered on every cell, so we can quantify spatial neighboring through increasing shared area between interaction circles of neighboring cells, where the closer the cells, the higher the overlapping area. Therefore if we use r=22 pixels (10 µm at 0.45 µm/pixel) as interaction radius, two cells will interact if they are closer than 1 diameter (44 pixels or 20 µm), since both cells have a circle of πr^2 around them), with a possible overlap going theoretically from 0 up to 100% (where upper limit is never reachable due to cell impossibility to compenetrate each other).
Lastly, we can build our own statistical overlapping test, by considering the chance of a pixel (i.e., an infinitesimal element of areal) being hit by an interaction circle of a cell as: a bernoulli event with success probability **p** given by: **p** = **a**/**A**, where **a** is the area of the interaction circle (πr^2 with r=44 pixels or 22 pixels, depending on the used threshold) and **A** is the total area of the available tissue (computed by measuring total interacting area covered by cells from the same sample).
Since **a**<<**A** we can ignore border effects on **A** and cell sizes, and now for each cell type pair **(i,j)** we can do the following:
Iff **j**=**i**:

- draw an interaction circle of area **a** for every cell of type **i**;
- measure $\mathbf{o_i}$ as the how many pixels are hit by at least 2 interaction circles;
- compare $\mathbf{o_i}$ with its asymptotic distribution under the null hypothesis, i.e. $\mathbf{o^{TH}_i}$ = *binomial*(**n**=$\mathbf{n_i}$, **p**=**a**/**A** , **k**>1) / *binomial*(**n**=$\mathbf{n_i}$, **p**=**a**/**A** , **k**>0), measurable using bootstrap methods, to estimate how likely would be for random cells to overlap as much as the observed ones for population **i**.

Iff **j**≠**i**:

- draw an interaction circle for every cell of type **i**, and for type **j**;
- define population areas $\mathbf{a_i}$ and $\mathbf{a_j}$ as all pixels hit by at least 1 cell of population **i** (or **j**);
- measure $\mathbf{o_{ij}} = |\mathbf{a_i} \cap \mathbf{a_j}| / |\mathbf{a_i} \cup \mathbf{a_j}|$;
- compare with *binomial*(**n**=*min*($\mathbf{n_i}$,$\mathbf{n_j}$) , **p**=*max*($\mathbf{a_i}$,$\mathbf{a_j}$)/**A** , **k** > $\mathbf{o_{ij}}$*min*($\mathbf{n_i}$,$\mathbf{n_j}$)).

By doing so, it is possible to estimate which cell types significantly overlap their interaction areas, and therefore are consistently neighboring with higher intensity than random.

Fisher significance test

Without elaborating in detail about a well-known test, we wish to highlight the difference between the Fisher test and the overlap method.
In the Fisher statistical test, we simply split cells in near cells and far cells, based on the selected distance threshold. Therefore there is no different contribution between two cells with different distances, as long as they are both within the threshold, or both outside the same.
What we are obtaining with the Fisher test is the odds ratio, or rather the ratio among the proportion inside and the proportion outside the neighborhood. So for a cell population which has 20% of its neighboring cells as B cells, while outside its neighborhoods there is a proportion of 5% B cells, it will result in an odds ratio of 20% / 5% = 4.
Since this measure can grow from 1 to infinity due to significant enrichments, but only span from 1 to 0 due to significant absences, it is used to symmetrize this by taking the logarithm of the odds ratios, resulting in a measure that goes from negative infinity up to positive infinity, with 0 as neutral (nor enriched nor absent population).

Distance

We further investigated cell interactions by taking another quantitative measure: the median distance from the nearest cell of a given type.
This measure has not an associated statistical test, therefore its only purpose was to quantify how far is usually the nearest cell of type B when we start from a cell of type A, and this is what is reported in Figure S10.

Significance of zonal distribution of cell subsets across zones.

The cell number and the zonal location for each cell type were computed. The “interstitial” type of distribution, not specific for a single LN zone, was not informative and therefore not included in the analysis from the regional point of view, but its cells were used for all enrichment tests as part of the “outside region” cells.
For each pair of region and cell type, a fisher test was conducted and results were aggregated as previously done for neighborhood tests: average odds ratios among different samples, consider as significant only those having consistently the same sign (always enriched or always depleted) with a max p value across samples lower than bonferroni corrected significance threshold. This allowed for the maximum possible control of false positives, stating as significant only cell types which were consistently and heavily enriched/depleted over the same region. Sample averaged significant odds ratios can be observed in Figure 7.

In order to further explore all available information, 2 more simple quantitative analyses were conducted: cell type relative distribution over available region, and average regional composition in terms of present cell types. Both can be observed in Figure 7. These analyses, even if not statistically validated, offer a view over cell types predisposition to occupy or not certain regions and viceversa, and combined with the enrichment test they provide a more complete information.

REFERENCES AND NOTES

1. Willard-Mack, C.L., *Normal structure, function, and histology of lymph nodes.* Toxicologic Pathology, 2006. **34**(5): p. 409-424 doi: 10.1080/01926230600867727. PMID: 17067937.http://eutils.ncbi.nlm.nih.gov/entrez/eutils/elink.fcgi?dbfrom=pubmed&id=17067937&retmode=ref&cmd=prlinks
2. Grant, S.M., et al., *The lymph node at a glance - how spatial organization optimizes the immune response.* Journal of Cell Science, 2020. **133**(5)10.1242/jcs.241828. PMID: 32144196.http://eutils.ncbi.nlm.nih.gov/entrez/eutils/elink.fcgi?dbfrom=pubmed&id=32144196&retmode=ref&cmd=prlinks
3. Conde, C.D., et al., *Cross-tissue immune cell analysis reveals tissue-specific features in humans.* Science (New York, NY), 2022. **376**(6594): p. eabl5197 doi: 10.1126/science.abl5197 PMID - 35549406.http://eutils.ncbi.nlm.nih.gov/entrez/eutils/elink.fcgi?dbfrom=pubmed&id=35549406&retmode=ref&cmd=prlinks
https://app.readcube.com/library/a0a2c82e-61ba-47f0-8ce9-1be84a3762b9/item/af87d741-642d-4fad-ac7a-affa9faa6173
4. Szabo, P.A., et al., *Single-cell transcriptomics of human T cells reveals tissue and activation signatures in health and disease.* Nature Communications, 2019. **10**(1): p. 4706 doi: 10.1038/s41467-019-12464-3. PMID: 31624246.http://www.nature.com/articles/s41467-019-12464-3
5. Rood, J.E., et al., *Impact of the Human Cell Atlas on medicine.* Nature Medicine, 2022. **28**(12): p. 2486-2496 doi: 10.1038/s41591-022-02104-7. PMID: 36482102.https://www.nature.com/articles/s41591-022-02104-7
6. Smet, F.D., A.A. Martinez, and F.M. Bosisio, *Next-Generation Pathology by Multiplexed Immunohistochemistry.* Trends in Biochemical Sciences, 2021. **46**(1): p. 80 - 82 doi: 10.1016/j.tibs.2020.09.009.http://eutils.ncbi.nlm.nih.gov/entrez/eutils/elink.fcgi?dbfrom=pubmed&id=33097382&retmode=ref&cmd=prlinks
https://app.readcube.com/library/a0a2c82e-61ba-47f0-8ce9-1be84a3762b9/item/9cc57c54-fb32-4ebd-bc98-a12affc07645
7. Leal, J.M., et al., *Innate cell microenvironments in lymph nodes shape the generation of T cell responses during type I inflammation.* Science Immunology, 2021. **6**(56)10.1126/sciimmunol.abb9435. PMID: 33579750.http://eutils.ncbi.nlm.nih.gov/entrez/eutils/elink.fcgi?dbfrom=pubmed&id=33579750&retmode=ref&cmd=prlinks
8. Stoltzfus, C.R., et al., *CytoMAP: A Spatial Analysis Toolbox Reveals Features of Myeloid Cell Organization in Lymphoid Tissues.* Cell reports, 2020. **31**(3): p. 107523 doi: 10.1016/j.celrep.2020.107523. PMID: 32320656.https://linkinghub.elsevier.com/retrieve/pii/S221112472030423X
9. Abe, Y., et al., *A single-cell atlas of non-haematopoietic cells in human lymph nodes and lymphoma reveals a landscape of stromal remodelling.* Nature Cell Biology, 2022. **24**(4): p. 565-578 doi: 10.1038/s41556-022-00866-3. PMID: 35332263.https://www.nature.com/articles/s41556-022-00866-3
10. Dall'Olio, L., et al., *BRAQUE: Bayesian Reduction for Amplified Quantization in UMAP Embedding.* Entropy (Basel), 2023. **25**(2): p. 354 doi: 10.3390/e25020354. PMID: 36832720.https://www.ncbi.nlm.nih.gov/pubmed/36832720
11. Furia, L., et al., *Automated multimodal fluorescence microscopy for hyperplex spatial-proteomics: Coupling microfluidic-based immunofluorescence to high resolution, high sensitivity, three-dimensional analysis of histological slides.* Front Oncol, 2022. **12**: p.

960734 doi: 10.3389/fonc.2022.960734. PMID: 36313693.https://www.ncbi.nlm.nih.gov/pubmed/36313693
12. Bolognesi, M.M., et al., *Multiplex Staining by Sequential Immunostaining and Antibody Removal on Routine Tissue Sections.* J Histochem Cytochem, 2017. **65**(8): p. 431-444 doi: 10.1369/0022155417719419. PMID: 28692376.https://www.ncbi.nlm.nih.gov/pubmed/28692376
13. Zou, D., et al., *CD4+ T cell immunity is dependent on an intrinsic stem-like program.* Nature Immunology, 2024. **25**(1): p. 66-76 doi: 10.1038/s41590-023-01682-z.https://app.readcube.com/library/a0a2c82e-61ba-47f0-8ce9-1be84a3762b9/item/13615812-afa3-4952-a49a-4b9ff76ba75e
14. Silva, J.G., et al., *Emergence and fate of stem cell–like Tcf7+ CD8+ T cells during a primary immune response to viral infection.* Science Immunology, 2023. **8**(89): p. eadh3113 doi: 10.1126/sciimmunol.adh3113.https://app.readcube.com/library/a0a2c82e-61ba-47f0-8ce9-1be84a3762b9/item/3684b433-81f8-4faf-93fc-9a12e1ada9da
15. Abadie, K., et al., *Reversible, tunable epigenetic silencing of TCF1 generates flexibility in the T cell memory decision.* Immunity, 2024. **57**(2): p. 271-286.e13 doi: 10.1016/j.immuni.2023.12.006.https://app.readcube.com/library/a0a2c82e-61ba-47f0-8ce9-1be84a3762b9/item/37f254cd-433e-48e5-911d-8e29cb87b67d
16. van Loosdregt, J., et al., *Canonical Wnt signaling negatively modulates regulatory T cell function.* Immunity, 2013. **39**(2): p. 298-310 doi: 10.1016/j.immuni.2013.07.019. PMID: 23954131.https://www.ncbi.nlm.nih.gov/pubmed/23954131
17. Hwang, S.-M., et al., *Inflammation-induced Id2 promotes plasticity in regulatory T cells.* Nature Communications, 2018. **9**(1): p. 4736 doi: 10.1038/s41467-018-07254-2. PMID: 30413714.http://www.nature.com/articles/s41467-018-07254-2
18. Cretney, E., et al., *The transcription factors Blimp-1 and IRF4 jointly control the differentiation and function of effector regulatory T cells.* Nature Immunology, 2011. **12**(4): p. 304-311 doi: 10.1038/ni.2006. PMID: 21378976
19. Wang, Z., et al., *PD-1hi CD8+ resident memory T cells balance immunity and fibrotic sequelae.* Science Immunology, 2019. **4**(36): p. eaaw1217 doi: 10.1126/sciimmunol.aaw1217. PMID: 31201259.http://immunology.sciencemag.org/lookup/doi/10.1126/sciimmunol.aaw1217
20. Sun, Q., et al., *BCL6 promotes a stem-like CD8+ T cell program in cancer via antagonizing BLIMP1.* Science Immunology, 2023. **8**(88): p. eadh1306 doi: 10.1126/sciimmunol.adh1306.https://app.readcube.com/library/a0a2c82e-61ba-47f0-8ce9-1be84a3762b9/item/5dfcfe5b-38ba-4863-a0ca-1a626a1cdc67
21. Ferreira, D.P., et al., *Central memory CD8+ T cells derive from stem-like Tcf7 hi effector cells in the absence of cytotoxic differentiation.* Immunity, 2020. **53**(5): p. 985-1000.e11 doi: 10.1016/j.immuni.2020.09.005.https://app.readcube.com/library/a0a2c82e-61ba-47f0-8ce9-1be84a3762b9/item/68f0b81c-0781-4002-a1f4-4ed42900c7fa
22. Schenkel, J.M. and K.E. Pauken, *Localization, tissue biology and T cell state - implications for cancer immunotherapy.* Nat Rev Immunol, 2023. **23**(12): p. 807-823 doi: 10.1038/s41577-023-00884-8. PMID: 37253877.https://www.ncbi.nlm.nih.gov/pubmed/37253877
23. Künzli, M. and D. Masopust, *CD4+ T cell memory.* Nature Immunology, 2023. **24**(6): p. 903-914 doi: 10.1038/s41590-023-01510-4.https://app.readcube.com/library/a0a2c82e-61ba-47f0-8ce9-1be84a3762b9/item/d7dd827f-8aff-46d6-bc7f-d85427875264
24. Caron, D.P., et al., *Multimodal hierarchical classification of CITE-seq data delineates immune cell states across lineages and tissues.* Cell Reports Methods, 2025. **5**(1): p. 100938 doi: 10.1016/j.crmeth.2024.100938.https://app.readcube.com/library/a0a2c82e-61ba-47f0-8ce9-1be84a3762b9/item/04ef59ff-5121-434d-a73e-55bd661f8a31

25. Miki, Y., et al., *Morphologic, flow cytometric, functional, and molecular analyses of S100B positive lymphocytes, unique cytotoxic lymphocytes containing S100B protein.* Eur J Haematol, 2013. **90**(2): p. 99-110 doi: 10.1111/ejh.12036. PMID: 23130680.http://eutils.ncbi.nlm.nih.gov/entrez/eutils/elink.fcgi?dbfrom=pubmed&id=23130680&retmode=ref&cmd=prlinks
26. Chang, Y., et al., *TGF-β specifies TFH versus TH17 cell fates in murine CD4+ T cells through c-Maf.* Science Immunology, 2024. **9**(93)10.1126/sciimmunol.add4818.https://app.readcube.com/library/a0a2c82e-61ba-47f0-8ce9-1be84a3762b9/item/ca002b93-274a-4860-90af-44dea6c86be4
27. Yasumizu, Y., et al., *Single-cell transcriptome landscape of circulating CD4+ T cell populations in autoimmune diseases.* Cell Genomics, 2024. **4**(2): p. 100473 doi: 10.1016/j.xgen.2023.100473.https://app.readcube.com/library/a0a2c82e-61ba-47f0-8ce9-1be84a3762b9/item/72573da6-b294-40f0-9ea6-eec6eb046038
28. Dann, E., et al., *Precise identification of cell states altered in disease using healthy single-cell references.* Nature Genetics, 2023. p. 1-11 doi: 10.1038/s41588-023-01523-7.https://app.readcube.com/library/a0a2c82e-61ba-47f0-8ce9-1be84a3762b9/item/059480df-ece6-45fc-abe5-6c432b063901
29. Deep, D., et al., *Precursor central memory versus effector cell fate and naïve CD4+ T cell heterogeneity.* Journal of Experimental Medicine, 2024. **221**(10): p. e20231193 doi: 10.1084/jem.20231193.https://app.readcube.com/library/a0a2c82e-61ba-47f0-8ce9-1be84a3762b9/item/e81037bd-8dd8-4b49-96af-0f22dbfad2df
30. Wu, Y.-C.B., D. Kipling, and D.K. Dunn-Walters, *The Relationship between CD27 Negative and Positive B Cell Populations in Human Peripheral Blood.* Frontiers in Immunology, 2011. **2**: p. 81 doi: 10.3389/fimmu.2011.00081.https://app.readcube.com/library/a0a2c82e-61ba-47f0-8ce9-1be84a3762b9/item/197f5cac-a0ad-4b6d-aa7c-4a72c0b3e5ce
31. Klein, U., K. Rajewsky, and R. Kuppers, *Human immunoglobulin (Ig)M+IgD+ peripheral blood B cells expressing the CD27 cell surface antigen carry somatically mutated variable region genes: CD27 as a general marker for somatically mutated (memory) B cells.* The Journal of experimental medicine, 1998. **188**(9): p. 1679-1689 doi. PMID: 9802980.http://www.ncbi.nlm.nih.gov/entrez/query.fcgi?cmd=Retrieve&db=PubMed&dopt=Citation&list_uids=9802980
32. Glass, D.R., et al., *An Integrated Multi-omic Single-Cell Atlas of Human B Cell Identity.* Immunity, 2020. **53**(1): p. 217-232.e5 doi: 10.1016/j.immuni.2020.06.013. PMID: 32668225.https://linkinghub.elsevier.com/retrieve/pii/S1074761320302685
33. Sims, G.P., et al., *Identification and characterization of circulating human transitional B cells.* Blood, 2005. **105**(11): p. 4390-4398 doi: 10.1182/blood-2004-11-4284.https://app.readcube.com/library/a0a2c82e-61ba-47f0-8ce9-1be84a3762b9/item/4c7eaa88-f6fb-4b62-a547-492f44a83146
34. Terekhova, M., et al., *Single-cell atlas of healthy human blood unveils age-related loss of NKG2C+GZMB−CD8+ memory T cells and accumulation of type 2 memory T cells.* Immunity, 2023.10.1016/j.immuni.2023.10.013.https://app.readcube.com/library/a0a2c82e-61ba-47f0-8ce9-1be84a3762b9/item/fdb2d317-1490-4054-a11a-c1e716afda86
35. Griffin, D.O., N.E. Holodick, and T.L. Rothstein, *Human B1 cells in umbilical cord and adult peripheral blood express the novel phenotype CD20+CD27+CD43+CD70−.* Journal of Experimental Medicine, 2011. **208**(1): p. 67-80 doi: 10.1084/jem.20101499.https://app.readcube.com/library/a0a2c82e-61ba-47f0-8ce9-1be84a3762b9/item/0d6f534b-ecf1-4554-bcdd-33ad875f9961
36. Stoler-Barak, L., et al., *B cell dissemination patterns during the germinal center reaction revealed by whole-organ imaging.* Journal of Experimental Medicine, 2019. **216**(11): p.

2515-2530 doi: 10.1084/jem.20190789. PMID: 31492809.http://eutils.ncbi.nlm.nih.gov/entrez/eutils/elink.fcgi?dbfrom=pubmed&id=31492809&retmode=ref&cmd=prlinks

37. Cattoretti, G., et al., *Stages of germinal center transit are defined by B cell transcription factor coexpression and relative abundance.* Journal of immunology (Baltimore, Md : 1950), 2006. **177**(10): p. 6930 - 6939 doi: 10.4049/jimmunol.177.10.6930.http://www.jimmunol.org/lookup/doi/10.4049/jimmunol.177.10.6930

https://app.readcube.com/library/a0a2c82e-61ba-47f0-8ce9-1be84a3762b9/item/b1b03adc-e877-44ae-9635-79129a34125f

38. Dameshek, W., *"Immunoblasts" and "Immunocyles"—An Attempt at a Functional Nomenclature.* Blood, 1963. **21**(2): p. 243-245 doi: 10.1182/blood.v21.2.243.243.https://app.readcube.com/library/a0a2c82e-61ba-47f0-8ce9-1be84a3762b9/item/ed117ee9-4d12-410b-8064-ddcaa7d6755f
39. van der Burg, M., C.M.R. Weemaes, and C. Cunningham-Rundles, *Chapter 16 - Isotype Defects*, in *Stiehm's Immune Deficiencies*, K.E. Sullivan and E.R. Stiehm, Editors. 2014, Academic Press: Amsterdam. p. 389-408.
40. Bain, V.G. and G.O. Bain, *Lymphocyte populations with abnormal kappa:lambda ratios in reactive lymphoid hyperplasia.* J Surg Oncol, 1985. **29**(4): p. 227-30 doi: 10.1002/jso.2930290406. PMID: 3935871.https://www.ncbi.nlm.nih.gov/pubmed/3935871
41. Faure, G.C., et al., *Plasma Cells Producing Lambda Light Chains Are Predominant in Human Gut and Tonsils: An Immunohistomorphometric Study.* American Journal of Clinical Pathology, 1990. **94**(5): p. 571-575 doi: 10.1093/ajcp/94.5.571 PMID - 2122717.http://eutils.ncbi.nlm.nih.gov/entrez/eutils/elink.fcgi?dbfrom=pubmed&id=2122717&retmode=ref&cmd=prlinks
42. Scott, G.D., et al., *Flow immunophenotyping of benign lymph nodes sampled by FNA: Representative with diagnostic pitfalls.* Cancer Cytopathol, 2018. **126**(9): p. 797-808 doi: 10.1002/cncy.22038. PMID: 30194715.https://www.ncbi.nlm.nih.gov/pubmed/30194715
43. Lorenzi, L., et al., *Immunoglobulin light chain transcript detection by ultrasensitive RNA in situ hybridization for B-cell lymphoma diagnosis.* Virchows Archiv, 2023. p. 1-9 doi: 10.1007/s00428-023-03682-8.https://app.readcube.com/library/a0a2c82e-61ba-47f0-8ce9-1be84a3762b9/item/42b9ee12-2d2c-451b-af47-bf512c056508
44. Ugur, M., et al., *Lymph node medulla regulates the spatiotemporal unfolding of resident dendritic cell networks.* Immunity, 2023.10.1016/j.immuni.2023.06.020.https://app.readcube.com/library/a0a2c82e-61ba-47f0-8ce9-1be84a3762b9/item/e22f9da2-f417-47b6-a386-c68ecbeeabf7
45. Haniffa, M., et al., *Human tissues contain CD141hi cross-presenting dendritic cells with functional homology to mouse CD103+ nonlymphoid dendritic cells.* Immunity, 2012. **37**(1): p. 60-73 doi: 10.1016/j.immuni.2012.04.012. PMID: 22795876.http://eutils.ncbi.nlm.nih.gov/entrez/eutils/elink.fcgi?dbfrom=pubmed&id=22795876&retmode=ref&cmd=prlinks
46. Cytlak, U., et al., *Differential IRF8 Transcription Factor Requirement Defines Two Pathways of Dendritic Cell Development in Humans.* Immunity, 2020. **53**(2): p. 353-370.e8 doi: 10.1016/j.immuni.2020.07.003. PMID: 32735845.https://linkinghub.elsevier.com/retrieve/pii/S1074761320302831
47. Villani, A.-C., et al., *Single-cell RNA-seq reveals new types of human blood dendritic cells, monocytes, and progenitors.* Science (New York, NY), 2017. **356**(6335)10.1126/science.aah4573. PMID: 28428369.http://eutils.ncbi.nlm.nih.gov/entrez/eutils/elink.fcgi?dbfrom=pubmed&id=28428369&retmode=ref&cmd=prlinks

48. Wood, G.S. and P.S. Freudenthal, *CD5 monoclonal antibodies react with human peripheral blood dendritic cells.* The American journal of pathology, 1992. **141**(4): p. 789-795 doi. PMID: 1384337.http://eutils.ncbi.nlm.nih.gov/entrez/eutils/elink.fcgi?dbfrom=pubmed&id=1384337&retmode=ref&cmd=prlinks
49. Granot, T., et al., *Dendritic Cells Display Subset and Tissue-Specific Maturation Dynamics over Human Life.* Immunity, 2017. **46**(3): p. 504-515 doi: 10.1016/j.immuni.2017.02.019. PMID: 28329707.http://eutils.ncbi.nlm.nih.gov/entrez/eutils/elink.fcgi?dbfrom=pubmed&id=28329707&retmode=ref&cmd=prlinks
50. Ulezko Antonova, A., et al., *A distinct human cell type expressing MHCII and RORγt with dual characteristics of dendritic cells and type 3 innate lymphoid cells.* Proceedings of the National Academy of Sciences, 2023. **120**(52): p. e2318710120 doi: 10.1073/pnas.2318710120. PMID: 38109523.https://app.readcube.com/library/a0a2c82e-61ba-47f0-8ce9-1be84a3762b9/item/8486fd45-85ef-438a-8ed5-6d2340878aa0
51. Lubin, R., et al., *The lifespan and kinetics of human dendritic cell subsets and their precursors in health and inflammation.* Journal of Experimental Medicine, 2024. **221**(11): p. e20220867 doi: 10.1084/jem.20220867.https://app.readcube.com/library/a0a2c82e-61ba-47f0-8ce9-1be84a3762b9/item/f1fc41c5-3930-41b4-b5a9-31877d6eeb8e
52. Boichuk, S.V., et al., *Gut-Associated Plasmacytoid Dendritic Cells Display an Immature Phenotype and Upregulated Granzyme B in Subjects with HIV/AIDS.* Frontiers in Immunology, 2015. **6**: p. 485 doi: 10.3389/fimmu.2015.00485.https://app.readcube.com/library/a0a2c82e-61ba-47f0-8ce9-1be84a3762b9/item/fa684f87-062b-4166-9294-182a3883002a
53. Facchetti, F., et al., *The plasmacytoid monocyte/interferon producing cells.* Virchows Archiv, 2003. **443**(6): p. 703-717 doi: 10.1007/s00428-003-0918-8. PMID: 14586652.http://www.ncbi.nlm.nih.gov/entrez/query.fcgi?cmd=Retrieve&db=PubMed&dopt=Citation&list_uids=14586652
54. Abramson, J., et al., *The emerging family of RORgammat(+) antigen-presenting cells.* Nat Rev Immunol, 2024. **24**(1): p. 64-77 doi: 10.1038/s41577-023-00906-5. PMID: 37479834.https://www.ncbi.nlm.nih.gov/pubmed/37479834
55. Shikhagaie, M.M., et al., *Neuropilin-1 Is Expressed on Lymphoid Tissue Residing LTi-like Group 3 Innate Lymphoid Cells and Associated with Ectopic Lymphoid Aggregates.* Cell Reports, 2017. **18**(7): p. 1761-1773 doi: 10.1016/j.celrep.2017.01.063.https://app.readcube.com/library/a0a2c82e-61ba-47f0-8ce9-1be84a3762b9/item/abd96621-ae52-4073-b33b-f7b6bc3980c3
56. Vivier, E., et al., *Innate Lymphoid Cells: 10 Years On.* Cell, 2018. **174**(5): p. 1054-1066 doi: 10.1016/j.cell.2018.07.017. PMID: 30142344.https://linkinghub.elsevier.com/retrieve/pii/S0092867418309115
57. Rigamonti, A., J. Villar, and E. Segura, *Monocyte differentiation within tissues: a renewed outlook.* Trends in Immunology, 2023. **44**(12): p. 999-1013 doi: 10.1016/j.it.2023.10.005.https://app.readcube.com/library/a0a2c82e-61ba-47f0-8ce9-1be84a3762b9/item/7810ec7d-ea39-499e-82e9-adb59d59db68
58. Zhao, J., I. Andreev, and H.M. Silva, *Resident tissue macrophages: Key coordinators of tissue homeostasis beyond immunity.* Sci Immunol, 2024. **9**(94): p. eadd1967 doi: 10.1126/sciimmunol.add1967. PMID: 38608039.https://www.ncbi.nlm.nih.gov/pubmed/38608039
59. Chakarov, S., et al., *Two distinct interstitial macrophage populations coexist across tissues in specific subtissular niches.* Science, 2019.

363(6432)10.1126/science.aau0964. PMID: 30872492.https://www.ncbi.nlm.nih.gov/pubmed/30872492

60. Bhutani, N., et al., *Reprogramming towards pluripotency requires AID-dependent DNA demethylation.* Nature, 2010. **463**(7284): p. 1042-1047 doi: 10.1038/nature08752. PMID: 20027182.https://www.nature.com/articles/nature08752
61. Trogisch, F.A., et al., *Endothelial cells drive organ fibrosis in mice by inducing expression of the transcription factor SOX9.* Science Translational Medicine, 2024. **16**(736)10.1126/scitranslmed.abq4581.https://app.readcube.com/library/a0a2c82e-61ba-47f0-8ce9-1be84a3762b9/item/0248b093-560c-49bd-a0c1-995678d6e410
62. Baptista, A.P., et al., *The Chemoattractant Receptor Ebi2 Drives Intranodal Naive CD4+ T Cell Peripheralization to Promote Effective Adaptive Immunity.* Immunity, 2019. **50**(5): p. 1188-1201.e6 doi: 10.1016/j.immuni.2019.04.001. PMID: 31053504.https://app.readcube.com/library/a0a2c82e-61ba-47f0-8ce9-1be84a3762b9/item/6456c905-0a45-4eca-97c0-3d1636b4f8c0
63. Giladi, A., et al., *Dissecting cellular crosstalk by sequencing physically interacting cells.* Nature Biotechnology, 2020. **38**(5): p. 629-637 doi: 10.1038/s41587-020-0442-2.https://app.readcube.com/library/a0a2c82e-61ba-47f0-8ce9-1be84a3762b9/item/2e3d9ed7-afae-4a4f-8103-5f021aafbbf9
64. Pasqual, G., et al., *Monitoring T cell–dendritic cell interactions in vivo by intercellular enzymatic labelling.* Nature, 2018. **553**(7689): p. 496-500 doi: 10.1038/nature25442. PMID: 29342141.https://app.readcube.com/library/a0a2c82e-61ba-47f0-8ce9-1be84a3762b9/item/d94f5b1d-9a2b-4888-9c60-4ef1bd5ee4ed
65. Steiner, T.M., W.R. Heath, and I. Caminschi, *The unexpected contribution of conventional type 1 dendritic cells in driving antibody responses.* European Journal of Immunology, 2022. **52**(2): p. 189-196 doi: 10.1002/eji.202149658. PMID: 34897660.http://eutils.ncbi.nlm.nih.gov/entrez/eutils/elink.fcgi?dbfrom=pubmed&id=34897660&retmode=ref&cmd=prlinks
66. Chappell, C.P., et al., *Extrafollicular B cell activation by marginal zone dendritic cells drives T cell-dependent antibody responses.* Journal of Experimental Medicine, 2012. **209**(10): p. 1825-1840 doi: 10.1084/jem.20120774. PMID: 22966002.http://eutils.ncbi.nlm.nih.gov/entrez/eutils/elink.fcgi?dbfrom=pubmed&id=22966002&retmode=ref&cmd=prlinks
67. Fitzgerald, D., et al., *A single-cell multi-omic and spatial atlas of nodal B-cell lymphomas reveals B-cell maturation drives intratumor heterogeneity.* 2024.10.1101/2023.11.06.565756.https://app.readcube.com/library/a0a2c82e-61ba-47f0-8ce9-1be84a3762b9/item/3d6d1495-c30f-4199-b303-2b5ccbf22c07
68. Goltsev, Y., et al., *Deep Profiling of Mouse Splenic Architecture with CODEX Multiplexed Imaging.* Cell, 2018. **174**(4): p. 968-981.e15 doi: 10.1016/j.cell.2018.07.010. PMID: 30078711.https://linkinghub.elsevier.com/retrieve/pii/S0092867418309048
69. Rahim, M.K., et al., *Dynamic CD8+ T cell responses to cancer immunotherapy in human regional lymph nodes are disrupted in metastatic lymph nodes.* Cell, 2023. **186**(6): p. 1127-1143.e18 doi: 10.1016/j.cell.2023.02.021 PMID - 36931243.https://app.readcube.com/library/a0a2c82e-61ba-47f0-8ce9-1be84a3762b9/item/0081ddbd-74a3-4722-9cc9-0cf99086dea7
70. D'Rozario, J., et al., *Fibroblastic reticular cells provide a supportive niche for lymph node–resident macrophages.* European Journal of Immunology, 2023. **53**(9): p. e2250355 doi: 10.1002/eji.202250355.https://app.readcube.com/library/a0a2c82e-61ba-47f0-8ce9-1be84a3762b9/item/fe650753-6b0f-43a6-9b3a-dae1a08e42e2
71. Pascual-Reguant, A., et al., *Multiplexed histology analyses for the phenotypic and spatial characterization of human innate lymphoid cells.* Nat Commun, 2021. **12**(1): p. 1737 doi:

10.1038/s41467-021-21994-8. PMID: 33741932.https://www.ncbi.nlm.nih.gov/pubmed/33741932
72. Girard, J.-P. and T.A. Springer, *High endothelial venules (HEVs): specialized endothelium for lymphocyte migration.* Immunology Today, 1995. **16**(9): p. 449-457 doi: 10.1016/0167-5699(95)80023-9.https://app.readcube.com/library/a0a2c82e-61ba-47f0-8ce9-1be84a3762b9/item/44ed3ca1-ff42-4365-bfcd-c637d91a5fa9
73. Cronin, D.M.P. and R.A. Warnke, *Castleman disease: an update on classification and the spectrum of associated lesions.* Advances in anatomic pathology, 2009. **16**(4): p. 236-246 doi: 10.1097/PAP.0b013e3181a9d4d3. PMID: 19546611.http://eutils.ncbi.nlm.nih.gov/entrez/eutils/elink.fcgi?dbfrom=pubmed&id=19546611&retmode=ref&cmd=prlinks
74. Cattoretti, G., et al., *Nuclear and cytoplasmic AID in extrafollicular and germinal center B cells.* Blood, 2006. **107**(10): p. 3967-3975 doi: 10.1182/blood-2005-10-4170. PMID: 16439679.http://eutils.ncbi.nlm.nih.gov/entrez/eutils/elink.fcgi?dbfrom=pubmed&id=16439679&retmode=ref&cmd=prlinks
75. van den Oord, J.J., et al., *Nodular alteration of the paracortical area. An in situ immunohistochemical analysis of primary, secondary, and tertiary T-nodules.* The American journal of pathology, 1985. **120**(1): p. 55-66 doi. PMID: 2409809.https://www.ncbi.nlm.nih.gov/pubmed/2409809
76. Tatsumi, N., et al., *Effective CD4 T cell priming requires repertoire scanning by CD301b+ migratory cDC2 cells upon lymph node entry.* Science Immunology, 2021. **6**(66): p. eabg0336 doi: 10.1126/sciimmunol.abg0336. PMID: 34890253.http://eutils.ncbi.nlm.nih.gov/entrez/eutils/elink.fcgi?dbfrom=pubmed&id=34890253&retmode=ref&cmd=prlinks
77. Cattoretti, G., et al. *Multiple Iterative Labeling by Antibody Neodeposition (MILAN)*. Protocol Exchange 2019 September 25, 2019; Available from: https://protocolexchange.researchsquare.com/article/nprot-7017/v5.
78. Bolognesi, M.M., et al., *Seeing or believing in hyperplexed spatial proteomics via antibodies: New and old biases for an image-based technology.* Biological Imaging, 2024. **4**: p. e10 doi: 10.1017/S2633903X24000138.https://www.cambridge.org/core/product/5FF0C706EA41AC1DB88D4C17ADB151CB
79. Ioachim, H.L., *Lymph Node Pathology*. 1994: J.B. Lipincott Company.
80. Schwartz, L.H., et al., *Evaluation of lymph nodes with RECIST 1.1.* European Journal of Cancer, 2009. **45**(2): p. 261-267 doi: 10.1016/j.ejca.2008.10.028.https://app.readcube.com/library/a0a2c82e-61ba-47f0-8ce9-1be84a3762b9/item/a7d5116b-fced-40ec-9ad4-1be4a8e9d956
81. Massoni-Badosa, R., et al., *An atlas of cells in the human tonsil.* Immunity, 2024. **57**(2): p. 379-399 e18 doi: 10.1016/j.immuni.2024.01.006. PMID: 38301653.https://www.ncbi.nlm.nih.gov/pubmed/38301653
82. Schwanhäusser, B., et al., *Global quantification of mammalian gene expression control.* Nature, 2011. **473**(7347): p. 337-342 doi: 10.1038/nature10098.https://app.readcube.com/library/a0a2c82e-61ba-47f0-8ce9-1be84a3762b9/item/1287f726-b955-4183-8178-ccacf6c5bba1
83. Su, E.Y., et al., *Direct comparison of mass cytometry and single-cell RNA sequencing of human peripheral blood mononuclear cells.* Scientific Data, 2024. **11**(1): p. 559 doi: 10.1038/s41597-024-03399-6.https://app.readcube.com/library/a0a2c82e-61ba-47f0-8ce9-1be84a3762b9/item/64fc5928-d090-4a4c-bebc-a0a8fb1afc14
84. Mahyari, E., et al., *Enhanced interpretation of immune cell phenotype and function through a rhesus macaque single-cell atlas.* Cell Genomics, 2025. p. 100849 doi:

10.1016/j.xgen.2025.100849.https://app.readcube.com/library/a0a2c82e-61ba-47f0-8ce9-1be84a3762b9/item/2c4ec3bd-5de8-4e9b-a0c4-4bdc62a7cbc5
85. Palm, A.-K.E., H.C. Friedrich, and S. Kleinau, *Nodal marginal zone B cells in mice: a novel subset with dormant self-reactivity.* Scientific reports, 2016. **6**: p. 27687 doi: 10.1038/srep27687. PMID: 27277419.http://eutils.ncbi.nlm.nih.gov/entrez/eutils/elink.fcgi?dbfrom=pubmed&id=27277419&retmode=ref&cmd=prlinks
86. Lazzi, S., et al., *IRTA1+ monocytoid B cells in reactive lymphadenitis show a unique topographic distribution and immunophenotype and a peculiar usage and mutational pattern of IgVH genes.* The Journal of Pathology, 2006. **209**(1): p. 56-66 doi: 10.1002/path.1944. PMID: 16508918
87. van den Oord, J.J., C. de Wolf-Peeters, and V.J. Desmet, *The marginal zone in the human reactive lymph node.* Am J Clin Pathol, 1986. **86**(4): p. 475-9 doi: 10.1093/ajcp/86.4.475. PMID: 3532758.https://www.ncbi.nlm.nih.gov/pubmed/3532758
88. van Krieken, J.H., et al., *Splenic marginal zone lymphocytes and related cells in the lymph node: a morphologic and immunohistochemical study.* Hum Pathol, 1989. **20**(4): p. 320-5 doi: 10.1016/0046-8177(89)90040-3. PMID: 2703226.https://www.ncbi.nlm.nih.gov/pubmed/2703226
89. Hunt, J.P., et al., *Hyperplasia of mantle/marginal zone B cells with clear cytoplasm in peripheral lymph nodes. A clinicopathologic study of 35 cases.* Am J Clin Pathol, 2001. **116**(4): p. 550-9 doi: 10.1309/P2M2-JEA3-YYQF-0P38. PMID: 11601140.https://www.ncbi.nlm.nih.gov/pubmed/11601140
90. Ruffin, A.T., et al., *Dysfunctional CD11c−CD21− extrafollicular memory B cells are enriched in the periphery and tumors of patients with cancer.* Science Translational Medicine, 2025. **17**(786): p. eadh1315 doi: 10.1126/scitranslmed.adh1315.https://app.readcube.com/library/a0a2c82e-61ba-47f0-8ce9-1be84a3762b9/item/cf0b8a6d-4c3f-43be-a200-80a5b3eb1be7
91. Shen, Q., et al., *TCF1 and LEF1 promote B-1a cell homeostasis and regulatory function.* Nature, 2025. p. 1-10 doi: 10.1038/s41586-025-09421-0.https://app.readcube.com/library/a0a2c82e-61ba-47f0-8ce9-1be84a3762b9/item/e591bc76-a4f1-4999-98f5-2ab4182d8865
92. Bolognesi, M.M., et al., *Antibodies validated for routinely processed tissues stain frozen sections unpredictably.* Biotechniques, 2021. **70**(3): p. 137-148 doi: 10.2144/btn-2020-0149. PMID: 33541132.https://www.ncbi.nlm.nih.gov/pubmed/33541132
93. Vercelli, D., et al., *Human recombinant interleukin 4 induces Fc epsilon R2/CD23 on normal human monocytes.* The Journal of experimental medicine, 1988. **167**(4): p. 1406-1416 doi: 10.1084/jem.167.4.1406. PMID: 2965737.http://eutils.ncbi.nlm.nih.gov/entrez/eutils/elink.fcgi?dbfrom=pubmed&id=2965737&retmode=ref&cmd=prlinks
94. Kawabe, T., et al., *Induction of Fc epsilon RII/CD23 on phytohemagglutinin-activated human peripheral blood T lymphocytes. I. Enhancement by IL-2 and IL-4.* The Journal of Immunology, 1991. **147**(2): p. 548-553 doi: 10.4049/jimmunol.147.2.548.https://app.readcube.com/library/a0a2c82e-61ba-47f0-8ce9-1be84a3762b9/item/fff7cdbb-1e4a-4c94-bb24-0ce75891dcad
95. Diggins, K.E., P.B. Ferrell, and J.M. Irish, *Methods for discovery and characterization of cell subsets in high dimensional mass cytometry data.* Methods (San Diego, Calif.), 2015. **82**: p. 55-63 doi: 10.1016/j.ymeth.2015.05.008. PMID: 25979346.http://eutils.ncbi.nlm.nih.gov/entrez/eutils/elink.fcgi?dbfrom=pubmed&id=25979346&retmode=ref&cmd=prlinks
96. Kanda, S., Y. Miyata, and H. Kanetake, *T-cell factor-4-dependent up-regulation of fibronectin is involved in fibroblast growth factor-2-induced tube formation by endothelial*

cells. Journal of Cellular Biochemistry, 2005. **94**(4): p. 835-847 doi: 10.1002/jcb.20354.https://app.readcube.com/library/a0a2c82e-61ba-47f0-8ce9-1be84a3762b9/item/65e49397-4850-4cac-aa46-c27620144a67

97. Crotty, S., R.J. Johnston, and S.P. Schoenberger, *Effectors and memories: Bcl-6 and Blimp-1 in T and B lymphocyte differentiation.* Nature Immunology, 2010. **11**(2): p. 114-120 doi: 10.1038/ni.1837. PMID: 20084069
98. Linterman, M.A., et al., *Foxp3(+) follicular regulatory T cells control the germinal center response.* Nature Medicine, 2011. **17**(8): p. 975-982 doi: 10.1038/nm.2425. PMID: 21785433.http://eutils.ncbi.nlm.nih.gov/entrez/eutils/elink.fcgi?dbfrom=pubmed&id=21785433&retmode=ref&cmd=prlinks
99. Conter, L., et al., *BLIMP1 controls GC B cell expansion and exit through regulating cell cycle progression and key transcription factors BCL6 and IRF4.* Cell Reports, 2025. **44**(7): p. 115977 doi: 10.1016/j.celrep.2025.115977.https://app.readcube.com/library/a0a2c82e-61ba-47f0-8ce9-1be84a3762b9/item/d3c742e6-2a76-4e6c-b6da-045bc87ff4ca
100. Salerno, F., et al., *An integrated proteome and transcriptome of B cell maturation defines poised activation states of transitional and mature B cells.* Nature Communications, 2023. **14**(1): p. 5116 doi: 10.1038/s41467-023-40621-2.https://app.readcube.com/library/a0a2c82e-61ba-47f0-8ce9-1be84a3762b9/item/4314ae14-5653-42ef-971b-48831287237d
101. Sciammas, R., et al., *Graded expression of interferon regulatory factor-4 coordinates isotype switching with plasma cell differentiation.* Immunity, 2006. **25**(2): p. 225-236 doi: 10.1016/j.immuni.2006.07.009. PMID: 16919487.http://www.ncbi.nlm.nih.gov/entrez/query.fcgi?cmd=Retrieve&db=PubMed&dopt=Citation&list_uids=16919487
102. Ochiai, K., et al., *Transcriptional regulation of germinal center B and plasma cell fates by dynamical control of IRF4.* Immunity, 2013. **38**(5): p. 918-29 doi: 10.1016/j.immuni.2013.04.009. PMID: 23684984.https://www.ncbi.nlm.nih.gov/pubmed/23684984
103. Küppers, R., et al., *Clonal composition and differentiation stage of human CD30+ B cells in reactive lymph nodes.* Frontiers in Immunology, 2023. **14**: p. 1208610 doi: 10.3389/fimmu.2023.1208610.https://app.readcube.com/library/a0a2c82e-61ba-47f0-8ce9-1be84a3762b9/item/c8d3b4c4-0357-4aa0-9a07-ecd613f94e1a
104. Weisel, N.M., et al., *Surface phenotypes of naive and memory B cells in mouse and human tissues.* Nature Immunology, 2022. **23**(1): p. 135-145 doi: 10.1038/s41590-021-01078-x. PMID: 34937918.http://eutils.ncbi.nlm.nih.gov/entrez/eutils/elink.fcgi?dbfrom=pubmed&id=34937918&retmode=ref&cmd=prlinks
105. Kisselgof, A.B. and H.C. Oettgen, *The expression of murine B cell CD23, in vivo, is regulated by its ligand, IgE.* International Immunology, 1998. **10**(9): p. 1377-1384 doi: 10.1093/intimm/10.9.1377.https://app.readcube.com/library/a0a2c82e-61ba-47f0-8ce9-1be84a3762b9/item/fdec1f22-39a6-4380-a89d-2f4a16c46978
106. Turner, C.T., D. Lim, and D.J. Granville, *Granzyme B in skin inflammation and disease.* Matrix Biol, 2019. **75-76**: p. 126-140 doi: 10.1016/j.matbio.2017.12.005. PMID: 29247692.http://eutils.ncbi.nlm.nih.gov/entrez/eutils/elink.fcgi?dbfrom=pubmed&id=29247692&retmode=ref&cmd=prlinks
107. Sporn, L.A., V.J. Marder, and D.D. Wagner, *von Willebrand Factor Released From Weibel-Palade Bodies Binds More Avidly to Extracellular Matrix Than That Secreted Constitutively.* Blood, 1987. **69**(5): p. 1531-1534 doi: 10.1182/blood.v69.5.1531.1531.https://doi.org/10.1182/blood.V69.5.1531.1531

https://app.readcube.com/library/a0a2c82e-61ba-47f0-8ce9-1be84a3762b9/item/2a1d6a32-5bd6-4ff3-96ec-1c15f05583ce
108. Villar, J. and E. Segura, *Decoding the Heterogeneity of Human Dendritic Cell Subsets.* Trends in Immunology, 2020. **41**(12): p. 1062-1071 doi: 10.1016/j.it.2020.10.002. PMID: 33250080.https://linkinghub.elsevier.com/retrieve/pii/S1471490620302313
109. Freud, A.G., et al., *The Broad Spectrum of Human Natural Killer Cell Diversity.* Immunity, 2017. **47**(5): p. 820-833 doi: 10.1016/j.immuni.2017.10.008. PMID: 29166586.http://linkinghub.elsevier.com/retrieve/pii/S1074761317304624
110. Ural, B.B., et al., *Inhaled particulate accumulation with age impairs immune function and architecture in human lung lymph nodes.* Nature Medicine, 2022. **28**(12): p. 2622-2632 doi: 10.1038/s41591-022-02073-x PMID - 36411343.https://app.readcube.com/library/a0a2c82e-61ba-47f0-8ce9-1be84a3762b9/item/32234bba-6374-4a52-8991-bb020e516561
111. Gretz, J.E., A.O. Anderson, and S. Shaw, *Cords, channels, corridors and conduits: critical architectural elements facilitating cell interactions in the lymph node cortex.* Immunological reviews, 1997. **156**: p. 11-24 doi: 10.1111/j.1600-065x.1997.tb00955.x. PMID: 9176696.https://www.ncbi.nlm.nih.gov/pubmed/9176696
112. Mungall, C.J., et al., *Uberon, an integrative multi-species anatomy ontology.* Genome Biol, 2012. **13**(1): p. R5 doi: 10.1186/gb-2012-13-1-r5. PMID: 22293552.https://www.ncbi.nlm.nih.gov/pubmed/22293552
113. Edfors, F., et al., *Enhanced validation of antibodies for research applications.* Nat Commun, 2018. **9**(1): p. 4130 doi: 10.1038/s41467-018-06642-y. PMID: 30297845.https://www.ncbi.nlm.nih.gov/pubmed/30297845
114. Mascadri, F., et al., *Rejuvenated Vintage Tissue Sections Highlight Individual Antigen Fate During Processing and Long-term Storage.* J Histochem Cytochem, 2021. **69**(10): p. 659-667 doi: 10.1369/00221554211047287. PMID: 34541944.https://www.ncbi.nlm.nih.gov/pubmed/34541944
115. Manzoni, M., et al., *The Adaptive and Innate Immune Cell Landscape of Uterine Leiomyosarcomas.* Scientific reports, 2020. **10**(1): p. 702-10 doi: 10.1038/s41598-020-57627-1. PMID: 31959856.http://www.nature.com/articles/s41598-020-57627-1
116. Furia, L., P.G. Pelicci, and M. Faretta, *A computational platform for robotized fluorescence microscopy (I): high-content image-based cell-cycle analysis.* Cytometry Part A : the journal of the International Society for Analytical Cytology, 2013. **83**(4): p. 333-343 doi: 10.1002/cyto.a.22266. PMID: 23463605.http://onlinelibrary.wiley.com/doi/10.1002/cyto.a.22266/full
117. Pelicci, S., et al., *Correlative Multi-Modal Microscopy: A Novel Pipeline for Optimizing Fluorescence Microscopy Resolutions in Biological Applications.* Cells, 2023. **12**(3): p. 354 doi: 10.3390/cells12030354. PMID: C737FDCE-95FA-4F60-AC22-041E9A60D8BE.https://www.mdpi.com/2073-4409/12/3/354
118. Mason, D.Y., et al., *Immunohistological analysis of human lymphoid tissue by double immunoenzymatic labelling.* Journal of Cancer Research and Clinical Oncology, 1981. **101**(1): p. 13-22 doi: 10.1007/bf00405059.https://app.readcube.com/library/a0a2c82e-61ba-47f0-8ce9-1be84a3762b9/item/02488003-0d87-4ed8-83aa-d08f4c98904a
119. Stringer, C., et al., *Cellpose: a generalist algorithm for cellular segmentation.* Nature methods, 2021. **18**(1): p. 100-106 doi: 10.1038/s41592-020-01018-x. PMID: 33318659.https://www.nature.com/articles/s41592-020-01018-x
120. Bai, Y., et al., *Adjacent Cell Marker Lateral Spillover Compensation and Reinforcement for Multiplexed Images.* Front Immunol, 2021. **12**: p. 652631 doi: 10.3389/fimmu.2021.652631. PMID: 34295327.https://www.ncbi.nlm.nih.gov/pubmed/34295327

121. Hao, Y., et al., *Integrated analysis of multimodal single-cell data.* Cell, 2021. **184**(13): p. 3573-3587.e29 doi: 10.1016/j.cell.2021.04.048. PMID: 34062119.http://eutils.ncbi.nlm.nih.gov/entrez/eutils/elink.fcgi?dbfrom=pubmed&id=34062119&retmode=ref&cmd=prlinks
122. Schindelin, J., et al., *Fiji: an open-source platform for biological-image analysis.* Nature methods, 2012. **9**(7): p. 676-682 doi: 10.1038/nmeth.2019. PMID: 22743772.http://eutils.ncbi.nlm.nih.gov/entrez/eutils/elink.fcgi?dbfrom=pubmed&id=22743772&retmode=ref&cmd=prlinks
123. Brbić, M., et al., *Annotation of spatially resolved single-cell data with STELLAR.* Nature methods, 2022. **19**(11): p. 1411-1418 doi: 10.1038/s41592-022-01651-8. PMID: 36280720.https://www.nature.com/articles/s41592-022-01651-8
124. Kaminski, A., et al., *Resident regulatory T cells reflect the immune history of individual lymph nodes.* Science Immunology, 2023. **8**(89): p. eadj5789 doi: 10.1126/sciimmunol.adj5789.https://app.readcube.com/library/a0a2c82e-61ba-47f0-8ce9-1be84a3762b9/item/8a2e6a48-fb04-4fe4-9ff4-1d625d7fb375
125. Roetman, J.J., et al., *Tumor-Reactive CD8+ T Cells Enter a TCF1+PD-1− Dysfunctional State.* Cancer Immunology Research, 2023. **11**(12): p. 1630-1641 doi: 10.1158/2326-6066.cir-22-0939.https://app.readcube.com/library/a0a2c82e-61ba-47f0-8ce9-1be84a3762b9/item/942b1695-76d8-45b4-875b-083223001263
126. Caron, D.P., et al., *Multimodal hierarchical classification of CITE-seq data delineates immune cell states across lineages and tissues.* bioRxiv, 2023. p. 2023.07.06.547944 doi: 10.1101/2023.07.06.547944.https://app.readcube.com/library/a0a2c82e-61ba-47f0-8ce9-1be84a3762b9/item/c98e0cc9-b169-4d87-b563-21bd8bccf576
127. Jarvis, L.B., et al., *Hiding in Plain Sight: Thymic CD8+FOXP3+Tregs sequester CD25 and are enriched in human tissues.* 2023.10.1101/2023.12.24.573232.https://app.readcube.com/library/a0a2c82e-61ba-47f0-8ce9-1be84a3762b9/item/62905420-f741-4368-858c-b2b715e6a470
128. Kitano, M., et al., *Imaging of the cross-presenting dendritic cell subsets in the skin-draining lymph node.* Proceedings of the National Academy of Sciences, 2016. **113**(4): p. 1044-1049 doi: 10.1073/pnas.1513607113.https://app.readcube.com/library/a0a2c82e-61ba-47f0-8ce9-1be84a3762b9/item/f535adc1-fe7a-47a3-a37b-66f9cfe8b091
129. Vinuesa, C., et al., *The transcription factors TCF1 and LEF1 drive B-1a cell development, self-renewal, and regulatory function.* 2024.10.21203/rs.3.rs-3855081/v1.https://app.readcube.com/library/a0a2c82e-61ba-47f0-8ce9-1be84a3762b9/item/1e2cec5d-bdfe-4a8e-b156-152dcb3b3467
130. Claireaux, M., et al., *Deep profiling of antigen-specific B cells from different pathogens identifies novel compartments in the IgG memory B cell and antibody-secreting cell lineages.* bioRxiv, 2023. p. 2023.12.19.572339 doi: 10.1101/2023.12.19.572339.https://app.readcube.com/library/a0a2c82e-61ba-47f0-8ce9-1be84a3762b9/item/ed048a38-f16b-40f3-9c92-8f09bb99167d
131. Villani, A.-C., et al., *Single-cell RNA-seq reveals new types of human blood dendritic cells, monocytes, and progenitors.* Science (New York, NY), 2017. **356**(6335)10.1126/science.aah4573.http://eutils.ncbi.nlm.nih.gov/entrez/eutils/elink.fcgi?dbfrom=pubmed&id=28428369&retmode=ref&cmd=prlinks https://app.readcube.com/library/a0a2c82e-61ba-47f0-8ce9-1be84a3762b9/item/d191710b-10db-4574-8dca-4e3d55aa20d2
132. Sulczewski, F.B., et al., *Transitional dendritic cells are distinct from conventional DC2 precursors and mediate proinflammatory antiviral responses.* Nat Immunol, 2023. **24**(8): p. 1265-1280 doi: 10.1038/s41590-023-01545-7. PMID: 37414907.https://www.ncbi.nlm.nih.gov/pubmed/37414907

133. Bourdely, P., et al., *Transcriptional and Functional Analysis of CD1c+ Human Dendritic Cells Identifies a CD163+ Subset Priming CD8+CD103+ T Cells.* Immunity, 2020. **53**(2): p. 335-352.e8 doi: 10.1016/j.immuni.2020.06.002. PMID: 32610077.https://linkinghub.elsevier.com/retrieve/pii/S1074761320302326
134. Girard, M., et al., *Type I interferons drive the maturation of human DC3s with a distinct costimulatory profile characterized by high GITRL.* Science Immunology, 2020. **5**(53): p. eabe0347 doi: 10.1126/sciimmunol.abe0347. PMID: 33188059.https://immunology.sciencemag.org/lookup/doi/10.1126/sciimmunol.abe0347
135. Yin, X., et al., *Human Blood CD1c+ Dendritic Cells Encompass CD5high and CD5low Subsets That Differ Significantly in Phenotype, Gene Expression, and Functions.* J Immunol, 2017. **198**(4): p. 1553-1564 doi: 10.4049/jimmunol.1600193. PMID: 28087664.https://www.ncbi.nlm.nih.gov/pubmed/28087664
136. See, P., et al., *Mapping the human DC lineage through the integration of high-dimensional techniques.* Science (New York, NY), 2017. **356**(6342): p. eaag3009 doi: 10.1126/science.aag3009. PMID: 28473638.http://www.sciencemag.org/lookup/doi/10.1126/science.aag3009
137. Dutertre, C.-A., et al., *Single-Cell Analysis of Human Mononuclear Phagocytes Reveals Subset-Defining Markers and Identifies Circulating Inflammatory Dendritic Cells.* Immunity, 2019. **51**(3): p. 573-589.e8 doi: 10.1016/j.immuni.2019.08.008. PMID: 31474513.https://linkinghub.elsevier.com/retrieve/pii/S1074761319303346
138. Leylek, R., et al., *Integrated Cross-Species Analysis Identifies a Conserved Transitional Dendritic Cell Population.* Cell reports, 2019. **29**(11): p. 3736-3750.e8 doi: 10.1016/j.celrep.2019.11.042. PMID: 31825848.https://linkinghub.elsevier.com/retrieve/pii/S2211124719315244
139. Narasimhan, H., et al., *Cross-species analyses reveal RORγt-expressing dendritic cells are a lineage of antigen presenting cells conserved across tissues.* bioRxiv, 2024. p. 2024.05.06.592772 doi: 10.1101/2024.05.06.592772.https://app.readcube.com/library/a0a2c82e-61ba-47f0-8ce9-1be84a3762b9/item/1ed88c71-b95e-4f6e-8da2-34c3dbc07ff0
140. Chakarov, S., et al., *Two distinct interstitial macrophage populations coexist across tissues in specific subtissular niches.* Science (New York, NY), 2019. **363**(6432)10.1126/science.aau0964.http://eutils.ncbi.nlm.nih.gov/entrez/eutils/elink.fcgi?dbfrom=pubmed&id=30872492&retmode=ref&cmd=prlinks https://app.readcube.com/library/a0a2c82e-61ba-47f0-8ce9-1be84a3762b9/item/bfcd9e4e-7ac0-4d8c-a334-c17937627c51
141. Alderson, M.R., et al., *Regulation of human monocyte cell-surface and soluble CD23 (Fc epsilon RII) by granulocyte-macrophage colony-stimulating factor and IL-3.* Journal of immunology (Baltimore, Md : 1950), 1992. **149**(4): p. 1252-1257 doi. PMID: 1386861.http://eutils.ncbi.nlm.nih.gov/entrez/eutils/elink.fcgi?dbfrom=pubmed&id=1386861&retmode=ref&cmd=prlinks
142. Krop, J., et al., *Imaging mass cytometry reveals the prominent role of myeloid cells at the maternal-fetal interface.* iScience, 2022. **25**(7): p. 104648 doi: 10.1016/j.isci.2022.104648. PMID: 35811852.http://eutils.ncbi.nlm.nih.gov/entrez/eutils/elink.fcgi?dbfrom=pubmed&id=35811852&retmode=ref&cmd=prlinks
143. Barros, M.H.M., et al., *Macrophage polarisation: an immunohistochemical approach for identifying m1 and m2 macrophages.* PLoS ONE, 2013. **8**(11): p. e80908 doi: 10.1371/journal.pone.0080908. PMID: 24260507.http://eutils.ncbi.nlm.nih.gov/entrez/eutils/elink.fcgi?dbfrom=pubmed&id=24260507&retmode=ref&cmd=prlinks

144. Ruco, L.P., et al., *Expression and cell distribution of the intercellular adhesion molecule, vascular cell adhesion molecule, endothelial leukocyte adhesion molecule, and endothelial cell adhesion molecule (CD31) in reactive human lymph nodes and in Hodgkin's disease.* The American journal of pathology, 1992. **140**(6): p. 1337-1344 doi. PMID: 1605306.http://eutils.ncbi.nlm.nih.gov/entrez/eutils/elink.fcgi?dbfrom=pubmed&id=1605306&retmode=ref&cmd=prlinks
145. Pusztaszeri, M.P., W. Seelentag, and F.T. Bosman, *Immunohistochemical expression of endothelial markers CD31, CD34, von Willebrand factor, and Fli-1 in normal human tissues.* The Journal of Histochemistry and Cytochemistry, 2006. **54**(4): p. 385-395 doi: 10.1369/jhc.4A6514.2005. PMID: 16234507
146. Park, S.M., et al., *Mapping the distinctive populations of lymphatic endothelial cells in different zones of human lymph nodes.* PLoS ONE, 2014. **9**(4): p. e94781 doi: 10.1371/journal.pone.0094781. PMID: 24733110.http://eutils.ncbi.nlm.nih.gov/entrez/eutils/elink.fcgi?dbfrom=pubmed&id=24733110&retmode=ref&cmd=prlinks

ACKNOWLEDGMENTS

We wish to thank Ulf Klein (School of Medicine, University of Leeds, UK), William Vermi and Silvia Lonardi (UNIBS, Brescia, Italy) for a critical review and suggestions, Cecilia Dominguez-Conde and Altea Gjurgjaj (Human Technopole, Milan, Italy) for help with data integration, Bachir Alobeid (Columbia U., USA), Carlo Parravicini (Ospedale L. Sacco, Milan, Italy), Asier Antoranz-Martinez, Lukas Marcelis, Thomas Tousseyn and Johanna Vets (KUL, Leuven, Belgium) for help in the early phase of this research.

FUNDING

Regione Lombardia POR FESR 2014–2020, Call HUB Ricerca ed Innovazione: ImmunHUB. (GCat and MMB)
EU Horizon 2020 programme (GenoMed4All project #101017549, HARMONY and HARMONY-PLUS project #116026) (GCast)
The AIRC Foundation (Associazione Italiana per la Ricerca contro il Cancro; Milan, Italy; projects #26216. (GCast)
KUL INTERNE FONDSEN MIDDEL-Zware infrastructuren EMH-D8191-AKUL/19/30 I005920N (FMB)
FWO Fundamenteel Klinisch Mandaat EMH-D8972-FKM/20. (FMB)
The National Recovery and Resilience Plan (NRRP), Mission 4 Component 2 Investment 1.4 - Call for tender No. 3138 of 16 December 2021, rectified by Decree n.3175 of 18 December 2021 of Italian Ministry of University and Research funded by the European Union – NextGenerationEU; Project code CN_00000033, Concession Decree No. 1034 of 17 June 2022 adopted by the Italian Ministry of University and Research, CUP B83C2200293000 , Project title “National Biodiversity Future Center - NBFC”. (MMB)

AUTHOR CONTRIBUTIONS

G.Catt, MMB, LDO and G.Cast designed the study.
GCatt and G.Cast supervised the work.
G.Catt and MMB performed experiments.
G.Catt, MMB, GEM annotated cells and slides.
LDO, SB, MF performed the computational analysis.
GCatt and G.Cast coordinated data generation.

G.Catt, FMB, AMH, LL, GB, MF provided clinical material or relevant resources.
G.Catt, MMB and LDO prepared the figures.
G.Catt, MMB and LDO wrote the manuscript.

COMPETING INTERESTS

The Authors declare no competing interests.

DATA AND MATERIALS AVAILABILITY

This publication is part of the Human Cell Atlas - www.humancellatlas.org/publications
Primary data (images .tif files, .csv files) have been deposited at the Human cell Atlas data portal: https://data.humancellatlas.org/

Analysis data have been deposited at UNIMIB Digital Commons repository Bicocca Open Archive Research Data (BOARD):
Bolognesi, Maddalena; Dall'Olio, Lorenzo; Borghesi, Simone; Castellani, Gastone; Cattoretti, Giorgio (2024), “The normal Lymph Node. BRAQUE analysis files & Raw Data”, Bicocca Open Archive Research Data, V1, doi: 10.17632/3ntbp3zdzh.1

The BOARD repository contains the following files/sub-folders:
- Supplementary data, tables, hi-res figures or figure parts
- BRAQUE analysis files: files produced by analyzing the data with BRAQUE
- Cell type subclassification: individual cell types analyzed with BRAQUE
- Neighborhood Analysis: neighborhood analysis on six whole LN
- CellPose2-segmentation: tissue segmentation with CellPose 2.0 and analysis with BRAQUE

Each sub-folder contains instructions and explanations for the content.
.ndpi acquisition image files are available upon request.

Any additional information required to reanalyze the data reported in this paper is available from the lead contacts upon request.
Giorgio Cattoretti: giorgio.cattoretti@unimib.it
Gastone Castellani: gastone.castellani@unibo.it

Declaration of generative AI and AI-assisted technologies

No generative AI and AI-assisted technologies were used for the preparation of this manuscript, in any section.

FIGURES AND TABLES

FIGURE LEGENDS

Figure1
Global single cell classification by BRAQUE in tissue sections.
A: The BRAQUE analysis pipeline. Right: sections of whole LN H&E images (WSI; scale bar = 5 mm. The TMA core, black image border, has a diameter of 2 mm). The images can be

examined at the link to https://tiny.cc/LNproject.The cartoon at the center depicts the cyclic staining and stripping MILAN method, followed by BRAQUE.
B: The UMAP virtual 2D map (left) and the real spatial distribution (right) of 727,729 cells, clustered with BRAQUE^{global}, is shown. Each cluster is color-coded. The scale on the left is virtual, the scale on the right are pixels (0.45µm/pixels). Case: UPN107.
C: The cell types identified in 27 LN samples (6 whole LN and 21 2mm TMA cores) after BRAQUE^{global} analysis on all cells in each sample, expressed as boxplots delimited by interquantile ranges, containing the median value (bar) and the mode (asterisk), whiskers indicating min/max values and individual sample points, including outliers. Data are reported in Table S3. Cells defined "T cells" and "B cells" cannot be further subdivided into subsets (see Table 1, Table S5).
D: The cell types identified in C are grouped as broad cell types, expressed as boxplots (see specification in Fig1C), excluded HDBSCAN -1, junk and unclassified from the calculation. Data are reported in Table S3.
E: The broad categories of CD4, CD8, B cells, dendritic and non-myeloid innate cells (DC) and myeloid cells shown in color in D was each separately analyzed by BRAQUE^{subclass} and each UMAP shown for UPN107 as an example. Images specifications are as per B.

Figure 2
T-cell classification and spatial distribution
A: Flowchart for the assignment of the TCF7 level category. Non-proliferating CD4 or CD8 T-cells are classified based on high, low and intermediate levels of TCF7, as depicted by the cluster signal intensity profile (red), compared to the sample population (blue).
B: Flowchart for the assignment of the subset type for CD4 and CD8 T-cell clusters upon subclustering. The presence/absence of subclassifying markers is drawn from the BRAQUE statistical output (see[10, 78])
C: Levels of TCF7 in CD4 and CD8 T-cell subsets.
TCF7 levels (high, average or low) are plotted for each CD4 and CD8 cell subtypes as percentage of clusters belonging to a subtype having that level.
D: Examples of spatial co-localization of T-cell subsets in whole LN sections. CD4 exhausted (red dots) and CD4 IFN response T-cells (blue dots) are examples of cell types with non-overlapping distribution. CD8 TCF7^{lo} (red dots) and CD8 IFN response T-cells (blue dots) are an example of neighboring cell types.
E: CD4 and CD8 neighborhood significant relationships. For each T-cell type the statistically significant neighbors are computed. Only significant values are plotted in shades of green as per the scale on the right. Note that CD4 with high or average TCF7 levels tend to be neighbors (red square). Activated and proliferating CD4 Treg, but not resting Treg also congregate together (pink square). CD8 effectors and exhausted are neighbors (orange square) as two CD8 subsets, CD8 TCF7^{lo} and CD8 IFN signal do (blue square). Average CD4 and CD8 represents HDBSCAN -1 clusters. 518,116 CD4 and 190,365 CD8 cells analyzed. The complete neighborhood and overlap chart can be seen in Figure 6.
F: CD4 and CD8 subtypes significant overlaps. CD4 with high or average TCF7 levels occupy overlapping spaces in the whole LN (red square); scale on the right. T_{reg} cell space, resting CD4 and activated or resting CD8, overlap with several other T-cell subsets. Note that previously noted (E) selected neighborhoods (pink, range and blue squares) do not correspond to spatial overlap regions.
G, H: CD4 and CD8 T-cells. T-cell types obtained after BRAQUE from five whole LNs represented as boxplots. For the boxplots specifications see Fig1.
I, K: CD4 and CD8 T-cell subtypes percentage composition of five whole lymph nodes.

Figure 3
B-cell classification and spatial distribution
A: B-cell types from five whole LNs represented as boxplots. For the boxplots specifications see Fig. 1. 1,443,539 cells analyzed.
Average B-cells are identified by default. MZ: mantle zone; CSR: class switch recombined.
B: B-cell subtypes percentage composition of five whole lymph nodes.
C: Spatial distribution of mature B-cell types, CD27+ or CD27neg. The spatial distribution of IgD+ B-cells and CSR B-cells is shown, divided according to the CD27 expression: negative in red, positive in blue. Overlapping cells are in black. The scale represents pixels (0.45 µm/pixel).
D: The Germinal Center (GC) environment components are shown for three whole LN. Five cell types are shown: centroblasts (red), proliferating ID2+ cells (green), MYC+ B-cells (orange), outer zone GC cells (OZ) (blue). The IgD+ MZ B-cells are shown to locate the B-cell follicle (turquoise). Note the extra follicular location of ID2+ Ki-67+ and MYC+ cells. Centrocytes are not shown. An area of each image is magnified as an inset. The scale represents pixels (0.45 µm/pixel).
E: Spatial distribution of CD5+ B-cell types. The spatial distribution of CD5+ MZ and CD5+ T-zone cells for five whole LN is shown in red. IgD+ CD27- MZ B-cells (blue) and the area occupied by naïve CD4 T-cells (yellow) are shown for spatial reference. Overlapping cells are in black. The scale represents pixels (0.45 µm/pixel). The complete neighborhood and overlap chart can be seen in Figure 6.
F: Spatial relationship between CD5+ Ig light chain+ B-cells and plasma cells. The CD5+ Ig light chain kappa+ and lambda+ (red) are spatially plotted together with the kappa and lambda positive plasma cells (blue). Cell overlap is in black.
G: Kappa/lambda ratio and plasma cell frequency from BRAQUE^{global}. The two-scale graph shows the kappa/lambda plasma cell ratio for 16 LN. The first six (darker columns) are whole LN, the remaining are TMA cores, six of them duplicates. The bars (scale on the left) show the k/l ratio. The triangle (scale on the right) the percentage of PC in each sample.
H: Comparison of the kappa/lambda ratio in plasma cells and in CD5+ light chain+ (LC) B-cells from BRAQUE^{subclass}.The k/l ratio of plasma cells (blue) is compared with the same ratio for CD5+ light chain+ B-cells (orange) in six whole LN.
I, K: Neighborhood and spatial cell overlap for mature B-cells. Note two domains for GC-related B-cells (red square): a mixture of centroblasts, MYC+ and proliferating ID2+ cells and a centroblast+centrocyte proper GC. CD5+ CD27^{negative} T1 B-cells (pink square) are neighbors, but do not have a common space allocation, although they share the space with MYC+ B-cells. CD27^{negative} B-cells (yellow square) and CD27+ ones (violet square) co-aggregate into separate neighborhoods and occupy mutually exclusive space domains. Plasma cells, plasmablasts and light chain+ CD5+ B1 cells co-aggregate and share the same space occupancy. Color scale is on the right.

Figure 4
Dendritic and innate immune cell classification and spatial distribution
A: Dendritic cell types from six whole LNs represented as boxplots. For the boxplots specifications see Fig1. Average DC are identified by default. 573,179 cells analyzed.
Abbreviations: cDC: conventional DC; DC mPh: DC with mixed phenotype; pDC: plasmacytoid DC; ILC3: innate lymphoid cells type 3; NK: natural killer cells. ID2+ Ki-67+ B-cells. macrophages and monocytes were misclassified as DC in the global analysis, but re-classified after BRAQUE^{subclass}.
B: DC subtypes percentage composition of six whole lymph nodes.

C: Seven DC subtypes are plotted, six of them as contrasting color-coded in pairs, spatially plotted. Cell overlap is in black.
D: Spatial distribution of ILC3 and pDC. ILC3 (red), pDC (green) and HEV (blue) are spatially plotted on six whole LN. The scale represents pixels (0.45 µm/pixel).
E: Paracortical aggregation of cDC2 (Fairy Circles, FC). **i:** Low power H&E stain (UPN104). The dotted outline highlights a paler area in the paracortex. A star labels a small GC surrounded by a MZ. Scale bar: 250µm. **ii:** a high magnification of the dotted area in **i** shows a polymorphic cell population composed of small lymphocytes, larger blasts, larger cells with a typical indented nucleus and ample clear cytoplasm and some HEV (arrows). Scale bar: 50 µm. **iii:** low power image of LN stained in immunofluorescence for CD1c (red), HLA-DR (green) and PNAd (white). Scale bar: 250 µm. **iv:** the dotted rectangular area in **iii** is magnified. A FC in the lower right is composed of cells with a dendritic appearance and a variegation of CD1c (red) and HLA-DR (green) double expression (yellow). On the upper left, a brightly green (DR+) small GC is surrounded by a red CD1c+ follicular MZ. PNAd+ HEV (blue) are surrounding and entering the FC. Scale bar: 500 µm. **v, vi, vii:** the individual immunofluorescence components of figure **iii** and **iv** are shown individually as a grayscale. Scale bar: 500 µm.
F: RGB and grayscale composite of a single cDC2-containing area. IF images for DAPI, CD5, CD1A, CD1c and CD4 are composed as RGB color images (top half). The figure bottom half contains inverted grayscale IF images of the same area, stained for 10 relevant antigens.The polygons are reproduced in identical locations across all the images and identify cDC2. Three CD5-stained cells centered on the triangles are magnified. Scale bar 50 µm.

Figure 5
Myeloid and stromal cell classification and spatial distribution
A: Myeloid cell types from six whole LN, shown as boxplots. For the boxplots specifications see Fig1. Average Myeloid cells are identified by default. 588,821 myeloid cells analyzed. Macs: macrophages; Act Macs: activated macrophages; PU1 cMAF: macrophages identified by high PU1 and cMAF.
B: Myeloid cell subtypes percentage composition of six whole lymph nodes.
C: The spatial distribution of CD23+ CD7+ GZMB+, GZMB+ and NK cells is shown on the outline of UPN107.
D: High magnification of an H&E detail of UPN107 (left) shows haemorragic effusion, prominence of HEV and scattered large blasts (black arrows). Another H&E detail (right) shows a marginal sinus containing scattered eosinophils (red arrows). Scale bar = 50 µm
E: Stromal cell types from six whole LN shown as frequency ±SD. The numbers next to the bars are the number of informative cases.
F: Stromal subtypes percentage composition of six whole lymph nodes represented as boxplots.
G: Spatial distribution of HEV (blue dots) and centrocytes (red dots) in four whole LN (left panel). Scales are pixels (0.45 µm/pixel). An H&E magnified representative field is shown in the right panel. The dotted white line highlights a germinal center, the arrows point to HEV. Scale bar 100 µm.

Figure 6
Neighborhood and cell type overlap
A: Neighborhood relationship between cell types. The figure contains all statistical significance values for each cell type (rows) versus the others (columns). Only the values equal or smaller than p 8.094544277157197e-06 (approx. 0.0000081) are shown. Color scale at the right.
B: Overlap for each cell type (rows) versus the others (columns). Only the values equal or smaller than p 8.094544277157197e-06 (approx. 0.0000081) are shown. Color scale at the right.

Figure 7
Distribution and statistical significance of cell types across the LN regions.
A: Relative distribution of each cell type across different regions. Each horizontal line sums up to 100%. Scale on the right.
B: Average region composition in terms of cell types. Each vertical column sums up to 100%. Scale on the right.
C: Significantly enriched/depleted cell types per region, showing average log odds ratios from Bonferroni corrected fisher tests. Scale on the right.
Data for UPN104-108.

TABLE LEGEND

Table 1
Description, tissue location, phenotype, numerosity of the cell types identified in six whole LN. Columns 4th to 6th show the marker frequency (by statistical relevance and by markers ranking) among clusters (i.e. marker-positive clusters/total clusters of that cell type), column 7th the top five markers with greater effect size. Highlighted in red in columns 4th to 6th are markers expressed in ≥70% of the cells of each cell type (i.e. total of cells positive for that biomarker/total cell of that cell type). Highlighted in bold in column 7th are the markers present in at least 30% of the cells of that type. The last column on the right contains the literature references with orthogonal validation of the phenotype. An expanded version with additional data (list of neighboring cell types and overlapping cells) is available as Supplementary Table 4.

Table 1

Cell type	Description	Location (% of cells)	Markers frequency in cell-type defined clusters (in red >70% of cells) 70-100%	50-69%	30-49%	Markers ranked 1st-5th (bold: >30% of clusters)	n. cells	n. clusters	UBERON	Othogonal validation Refs.
CD4									CL:0000084	
CD4 naïve-like	TCF7hi naïve CD4	paracortex (50-70%);	TCF7	GATA3, MYC	BCL6, CD30, cMAF, ID2, PRDM1	CD69, CD74, CD86, CXCL13, GATA3, IRF4, PD1, PDL1, S100B, TCF7, TOX1	145,523	25	CL:0000895	[22, 81]
CD4 poised	TCF7hi CD4 with co-inhibitory receptors	paracortex (≥70%);	GATA3, GZMB, TCF7	CD137, MYC, TIM3	BCL6, CD30, CD69, CD86, LAG3, OX40, PD1, PDL1, PRDM1	CD86, IRF4, TCF7	129,010	24		[22, 29]
CD4 proliferating	Proliferating CD4	interstitial, paracortex, medullary cords (20-50%)	ID2, Ki-67, TOX1	BCL6, IRF4, MX1, MYC, PRDM1	CD56, CD69, CD86, CXCL13	**CD69, ID2, Ki-67**	13,484	14		[81]
CD4 effector	CD4 with activation and co-inhibitory receptors, TCF7avg (not low)	paracortex, medullary cords (20-50%)		CD56, CD69, OX40, PD1, TIM3	CD23, CD86, CD137, cMAF, CXCL13, GZMB, IRF4, MYC, PDL1, PRDM1, TOX1	**CD86**	127,683	55		[22]
CD4 effector S100B+	S100B+ CD4 with activation and co-inhibitory receptors	paracortex (≥70%);	CD56, CD69, OX40, PDL1, S100B, TIM3	CD23, CD103, HLADR, IRF4, PD1	CD86, cMAF, CXCL13, MYC	**HLADR**	36,117	30		
CD4 exhausted	TCF7low CD4 with multiple exhaustion markers	medullary cords, Activation spot (20-50%) May be focal	CD56, CD86, CD103, GZMB, MYC, OX40, PD1	CD137, LAG3, MX1	CD23, CD30, CD69, CD74, CXCL13, EOMES, PRDM1, RORC, TIM3, TOX1	CD23, CD69, GZMB, IRF4	17,193	15		[22]
CD4 IFN response	MX1+ CD4	paracortex (≥70%); May be focal	MX1		CD56, CXCL13, TCF7	CD69, CD74, CD86, cMAF, CXCL13, GATA3, MX1, OX40, TCF7, TIM3	44,546	15		[27, 29]
CD4 Treg resting	FOXP3+ Regulatory CD4; also	interstitial (≥70%);	FOXP3	CD30, MX1, TIM3, TOX1	BCL6, CD56, CD86, cMAF, GATA3, ID2,	CD30, CXCL13, FOXP3, PDL1, PRDM1	50,180	16	CL:0000815	[17, 124]

	named "central" Tregs				PRDM1					
CD4 Treg activated	FOXP3+ Regulatory CD4 with activation or co-inhibitory receptors; also named "effectors" Tregs	interstitial (≥70%);	FOXP3, GATA3, IRF4, PRDM1, TIM3	CD69, CD86, cMAF, OX40, PD1, TOX1	BCL6, CD23, CD30, CD56, GZMB, ID2, MX1, MYC, PDL1	FOXP3, S100B	96,405	41	CL:0000815	[17, 18, 124]
CD4 Treg S100B+ activated	FOXP3+ S100B+ Regulatory CD4 with activation/co-inhibitory recept.	paracortex (≥70%);	CD69, FOXP3, IRF4, OX40, PDL1, PRDM1, S100B, TIM3	GATA3, HLADR	CD23, CD56, CD86, cMAF, MX1, TOX1	**FOXP3, HLADR**	6,403	17	CL:0000815	[18]
CD4 Treg proliferating	Proliferating FOXP3+ Regulatory CD4	paracortex (50-70%); interstitial (20-50%)	FOXP3, GATA3, ID2, IRF4, Ki-67, PRDM1, TOX1	cMAF, MX1	BCL6, CD86, MYC, TIM3	**FOXP3, Ki-67**	6,735	19	CL:0000815	[17, 26]
CD4 Tfh	Follicular T helper cells	follicular (≥70%);	BCL6, CD56, CD69, CD137, CXCL13, ID2, Ki-67, PD1, TOX1	cMAF	CD30, CD86, MX1	**BCL6, PD1, TOX1**	6,818	9	CL:0002038	[26, 81]
CD4 undefined	CD4 of uncertain phenotype	interstitial, paracortex, regional distr. (20-50%)			CD30, cMAF	BCL6, CD69, CD74, cMAF, CXCL13	13,599	8		
Average CD4	Default assignment by BRAQUE	NA (≥70%);	MX1	TCF7, TOX1	CD30, CD56, cMAF, CXCL13, GATA3, GZMB, ID2, IRF4, Ki-67, PD1, TIM3	CD86, cMAF, FOXP3, PDL1, TCF7	66,918	4		
CD8									CL:0000084	
CD8 naïve-like	TCF7hi/avg Naïve CD8	interstitial (50-70%); paracortex (20-50%)		BCL6, TCF7	CD69, cMAF, CXCL13, GATA3,	BCL6, CD16, CD69, CD86, cMAF, CXCL13, RORC, TCF7	45,890	42	CL:0000900	[14, 22, 69]

PRDM1

CD8 poised	TCF7hi Naïve CD8 with co-inhibitory receptors; also named Tresident memory	interstitial (50-70%); paracortex (20-50%)	CD23, MYC, PD1, PRDM1, TCF7	CD137, CXCL13, GATA3, GZMB, OX40	BCL6, CD69, CD86, ID2, LAG3, TIM3	CD56, CD74, CD86, cMAF, PD1, TCF7, TOX1	6,993	10		[14, 21, 22, 69, 81, 125]
CD8 S100B+ naïve like	S100B+ TCF7hi Naïve CD8	interstitial (≥70%);		BCL6, CXCL13, MYC, OX40, PD1, PRDM1, S100B, TCF7		**MYC, S100B, TCF7**	3,171	2		[25, 126]
CD8 S100B+ other	S100B+ CD8 with co-inhibitory receptors; any TCF7, any FOXP3	interstitial (≥70%);	CD86, S100B, TIM3	FOXP3, GATA3, HLADR, IRF4, MYC, OX40, PDL1, PRDM1, TCF7	BCL6, CD23, CD56, CD137, CXCL13, GZMB, ID2, LAG3	CD86, EOMES, HLADR, S100B	16,246	10		[25, 126]
CD8 proliferating	Proliferating CD8, any TCF7 value	interstitial (50-70%); medullary cords (20-50%)	Ki-67	CD86, EOMES, ID2, IRF4, PRDM1, TIM3	BCL6, GATA3, MX1, MYC, TOX1	BCL6, CD30, CD103, EOMES, ID2, Ki-67	4,361	12		[69, 81]
CD8 effector	CD8 with co-inhibitory receptors, TCF7avg (not hi, neither low); also named Progenitor Exhausted	interstitial, medullary cords (20-50%)		CD23, CD137, GZMB, OX40, PD1, PDL1, PRDM1, TIM3	CD16, CD56, CD74, CD86, ID2, MYC	HLADR, IRF4, LAG3	34,312	29		[14, 22, 69, 81, 125]
CD8 exhausted	TCF7low CD8 with multiple co-inhibitory receptors	interstitial (50-70%); medullary cords (20-50%)	GZMB	CD23, PD1	CD69, CD74, CD137, MYC, OX40, TIM3, TOX1	CD74, CD103, GZMB, PD1, S100B, TIM3	18,715	23	CL:0000910	[14, 69]
CD8 IFN response	MX1+ CD8, any TCF7 value	interstitial, capsular (20-50%)	MX1	cMAF	CD74, CD86, CXCL13, TIM3	BCL6, CD69, CD74, CD86, cMAF, CXCL13, EOMES, MX1	10,807	13		[81]

CD8 TCF7lo	TCF7low with a naïve phenotype	interstitial, paracortex (20-50%)		CD69, CXCL13	cMAF, TIM3	BCL6, CD69, CD74, CD86, cMAF, CXCL13, EOMES, ID2, PDL1, TOX1	3,776	16		
CD8 Treg resting	FOXP3+ TCF7hi/avg Regulatory CD8, resting	paracortex (50-70%); interstitial (20-50%)	FOXP3	CD69, GATA3, PRDM1, TCF7	CXCL13, LAG3, TOX1	**FOXP3, GATA3, PRDM1, TCF7**	4,239	6		[127]
CD8 Treg activated	FOXP3+ Regulatory CD8 with activation	interstitial (≥70%); paracortex (20-50%)	FOXP3, TIM3	CD69, CD86, GATA3, IRF4, PD1, PRDM1, TOX1	CD74, CD137, ID2, LAG3, MX1	CD56, CD137, EOMES, FOXP3	4,172	8		[18, 127]
CD8 undefined	CD8 of uncertain phenotype	medullary cords (50-70%); interstitial (20-50%)				CD86	6,563	25		
Average CD8	Default assignment by BRAQUE	NA (≥70%);		CXCL13, MX1	OX40, PD1, PDL1, TIM3	CD69, CD86, MX1, PRDM1, S100B, TCF7, TOX1	31,120	5		
B cells									CL:0000236	
ID2+ Ki-67+ B cells	ID2+ Proliferating B cells	GC + scattered (50-70%); interstitial (20-50%)	BCL6, ID2, Ki-67, TOX1	AID, CD86, PAX5	CD10, CD20, CD74, HLADR, IRF8, MYC, PRDM1, PU1, TCF7	BCL6, CD79a, ID2, Ki-67	18,315	18		[81, 128]
MYC+ B cells	MYC+ B cells	interstitial, marginal zone (20-50%)	MYC	CD74, CD86, IRF8, PRDM1, TCF7	AID, BCL2, BCL6, CD1c, CD5, CD20, CD21, CD79a, Ki-67, PAX5, PDPN, PU1, TOX1	BCL6, IgD, IRF4, Ki-67, MYC, TOX1	19,326	9		[81]
Centroblasts	GC dark-zone proliferating B cells	follicular (≥70%);	AID, BCL6, CD10, CD20, CD21, CD74, CD86, HLADR, ID2, IRF8, Ki-67, PAX5, PDPN, PU1, TOX1	CD23	MX1, PRDM1	**BCL6, CD21, Ki-67**	96,464	91	CL:0009112	[81]
Centrocytes	GC light-zone B cells	follicular (≥70%);	CD20, CD21, CD23, CD86, PDPN, TOX1	AID, BCL6, CD10, CD69, CD74,	CD11c, ID2, IRF8, PAX5, PU1	CD1c, CD21, CD23, IRF4, PDPN, PRDM1	35,677	30	CL:0009111	[81]

				HLADR						
CD5+ MZ	CD5+ mature B cells, coexpressing PAX5 and TCF7	marginal zone (50-70%); follicular (20-50%)	CD5, TCF7	BCL2, TOX1	AID, CD11c, CD23, CD27, CD69, CD74, IRF8, MYC, PDPN, PRDM1, PU1	BCL2, CD5, CD27, IgD, IRF8, lambda	125,346	38		[32, 34, 129]
CD5+ T-zone cells	CD5+ TCF7+ B cells	paracortex NOS (20-50%)	BCL6, CD5, CD86, PRDM1, TCF7	IRF4, MYC	CD1c, CD11c, HLADR, ID2, TOX1	CD1c, ID2, IRF4, MX1, TCF7	56,274	22		[32, 34, 81, 129]
IgD+ CD27neg	IgD+ mature B cells residing in the follicular mantle zone	follicular (≥70%);	CD20, CD79a, IgD, PAX5, PU1	CD1c, CD74, HLADR, MX1	BCL2, IRF8, PDPN	CD79a, IgD, IRF4	384,855	122	CL:0000788	[31, 81, 104, 130]
CSR CD27neg	Mature B cells, IgDneg CD27 neg residing in the follicular mantle zone	follicular (≥70%);	CD74	BCL2, CD79a, PU1	CD1c, CD20, CD21, IRF8, MX1, PAX5, PDPN	CD1c, CD11c, CD20, CD21, CD23, IRF8, kappa, lambda, PDPN, PU1	139,665	42	CL:0000788	[31, 90, 104, 130]
IgD+ CD27+	CD27+ mature B cells, IgD+	medullary cords (50-70%);	BCL2, CD20, CD23, CD27, CD79a, IgD	IRF8, MYC, PRDM1, PU1	CD74	BCL2, CD21, CD69, CD86, HLADR, IRF8	42,066	17	CL:0000787	[31, 81, 104, 130]
CSR CD27+	CD27+ mature B cells, IgDneg	medullary cords (≥70%);	BCL2, CD20, CD23, CD27	CD5, CD74, CD79a, IRF8, MYC, PRDM1, TOX1	AID, CD69, PU1	BCL2, CD21, CD27, CD69, IRF8	72,064	17	CL:0000787	[31, 81, 104, 130]
immunoblasts	Activated mature B cells	interstitial (20-50%)	CD5, CD69, IRF4, MYC, PRDM1	BCL2, CD27, TCF7		CD5, CD30, IRF4, Ki-67, MYC, TCF7	4,931	6		[81]
PC kappa	Plasma cells kappa	medullary cords (≥70%);	CD27, CD69, IRF4, kappa, PRDM1	CD11c, CD23, CD86, ID2, MYC	AID, CD5, CD10, MX1, PDPN, TCF7, TOX1	**IRF4, kappa, PRDM1**	63,474	30	CL:0000786	[81]
PC lambda	Plasma cells lambda	medullary cords (≥70%);	CD27, IRF4, lambda, PRDM1	AID, CD23, CD69	CD5, CD10, CD11c, ID2, MYC, PDPN, TOX1	**IRF4, lambda, PRDM1**	48,072	27	CL:0000786	[81]
plasmablasts	Immature plasma cells	marginal zone, GC + scattered (20-50%)	IRF4, Ki-67, PRDM1	ID2, kappa, lambda, MX1, MYC	AID, BCL6, CD27, CD86, TOX1	ID2, IRF4, Ki-67, lambda, PRDM1	2,161	6	CL:0000980	[81, 130]

CD5+ kappa	CD5+ CD27+ mature B cells, Ig light chain positive	medullary cords (≥70%);	CD5, CD27, kappa, PRDM1, TCF7	CD11c, CD69	AID, BCL2, CD23, IRF4, MX1, MYC	CD1c, CD27, kappa	56,728	15		[32, 35, 81, 129, 130]
CD5+ lambda	CD5+ CD27+ mature B cells, Ig light chain positive	medullary cords (≥70%);	CD5, CD27, lambda, TCF7	AID, CD11c, CD69, PRDM1	CD23, IRF4, MX1, TOX1	CD1c, CD5, CD27, CD86, IRF8, lambda	43,704	26		[32, 35, 81, 129, 130]
IFNsignal B	Mature B cells with evidence of IFN signaling	marginal/subcapsular z., follicular (20-50%)	MX1	CD20	BCL2, CD74, HLADR	BCL2, CD1c, CD10, CD11c, CD20, CD27, CD86, ID2, IRF8, lambda, MX1	20,036	16		[81]
Undefined B cells	B cells of uncertain phenotype	marginal zone (20-50%)		lambda	AID, CD10, CD11c, CD27, CD69, CD86, ID2, IRF4, MYC, PDPN, PRDM1	CD21, CD74, IRF4, kappa, lambda, PU1	35,193	28		
Average B cells	Default assignment by BRAQUE		CD5, CD11c, MYC	AID, CD23, CD69, HLADR, TOX1	CD21, CD30, CD74, CD79a, IRF8, lambda, MX1, PDPN, PRDM1, TCF7	CD11c, CD86, IgD	179,345	6		
DC									CL:0000451	
cDC1A	Conventional Dendritic Cell type 1, full phenotype	interstitial, paracortex (20-50%)	CD74, CD141, CLEC9A, IDO, LYZ, TIM3	BCL6, CD11c, HLADR, MYC, PU1	CD4, CD31, CD86, IRF8, MYCN, RORC	**IRF8, PU1, TIM3**	31,451	51	CL:0002394	[81, 131]
cDC1B	Conventional Dendritic Cell type 1, partial phenotype	paracortex, medullary cords (20-50%)	CD141	CD4, CD86, CD303, CLEC9A, MYC, PRDM1	BCL2, BCL6, CD5, CD7, CD11c, CD16, HLADR, IDO, MYCN, PDL1, TIM3	CD11c, CD86, cMAF, HLADR, OX40	33,312	17	CL:0002394	[81, 131]
cDC1 prolif	proliferating conventional Dendritic Cell type 1	interstitial (≥70%); paracortex (20-50%)	BCL6, CD74, CD141, CLEC9A, ID2, IRF8, Ki-67, LYZ, MYC, PU1, RORC, TIM3	IDO	HLADR, MX1, PRDM1	BCL6, IRF8, PU1, PDL1	1,484	5		[81]

cDC2A	Conventional Dendritic Cell type 2, CD207+ CD5neg	paracortex (50-70%); interstitial (20-50%)	CD1A, CD86, CD207, HLADR, IRF4	BCL6, CD1c, CLEC9A, PU1, RORC	CD74, PDL1, S100B	**CD103, CD207, IRF4, PU1, S100B**	17,958	32	CL:0002399	[45, 81]
cDC2A CD5+	conventional Dendritic Cell type 2, CD207+ CD5+	paracortex (≥70%);	CD1A, CD4, CD5, CD86, CD207, CLEC9A	BCL2, CD1c, CD45, HLADR, PRDM1, PDL1, S100B	CD7, MYC, OX40	**CD1A, CD207**	34,731	50	CL:0002399	[45-47, 81, 132-138].
cDC2B	Conventional Dendritic Cell type 2, CD207neg, CD5neg	interstitial, paracortex, capsular (20-50%)	CD86, IRF4, PU1	CD1c, HLADR	BCL6, PDL1, RORC, TIM3	AXL, CD31, CD45, HLADR, IRF4, PU1, S100B	15,921	23	CL:0002399	[46, 47, 81, 132-138].
cDC2B CD5+	Conventional Dendritic Cell type 2, CD207neg, CD5+	paracortex (≥70%);	BCL2, CD4, CD5, CD86, HLADR, PRDM1	CD1c, CD7, CLEC9A, MYC, PDL1	CD1A, CD45, IDO, IRF4, MYCN, S100B	CD86, cMAF, HLADR, IRF4, OX40, PU1	24,007	36	CL:0002399	[46, 47, 81, 132-138].
DCmPh	Conventional Dendritic Cell, mixed type 1 and 2 phenotype	paracortex (50-70%);	TIM3	CD1c, CD11c, CD45, CD86, CD141	AXL, BCL6, CD4, CD74, CD207, cMAF, CLEC9A, CLEC10A, HLADR, LYZ, MYC, MYCN, OX40, PRDM1, PU1, PDL1, RORC	HLADR, IRF4, PU1, S100B	42,247	47		[45, 49, 136]
ID2+ Ki-67+	ID2+ Proliferating cells, non T, non B	interstitial (≥70%);	ID2, Ki-67, PRDM1	MYC	AXL, BCL6, cMAF, IRF4, PU1	BCL2, CD16, ID2, IRF4, Ki-67, PRDM1	19,943	13		
pDC	Plasmacytoid Dendritic cells	interstitial, paracortex, medullary cords (20-50%)	CD303, IRF8, MX1, TCF4	CD31, CD74	CD68, CLEC10A, IRF4	CD86, IDO, IRF8, TCF4	63,090	37	CL:0001058	[47, 81]
ILC3	Innate lymphoid cells type 3	interstitial (50-70%); paracortex (20-50%)	PU1, RORC	CD11c, CD74, CLEC10A	AXL, CD1c, CD45, LYZ, MYC, TIM3	CD1c, CD11c, IRF4, IRF8, PU1, RORC, S100B	46,938	45		[50, 54, 139]
NK	Natural killer cells	paracortex (50-70%);	CD16, CD56	CD7, CD31, CLEC10A, MYC	AXL, CD5, HLADR, IDO, MYCN, OX40, S100B	**CD56, CLEC10A, HLADR, OX40**	8,821	19	CL:0000623	[56, 81]

DC undefined	DC cells of uncertain phenotype	paracortex, medullary cords (20-50%)		BCL2, CD5, MYC	AXL, CD4, CD7, CD45, CLEC9A, CLEC10A, HLADR, MYCN, PRDM1	CD4, CD5, CD11c, CD86, CD303, HLADR, IDO, IRF4, IRF8, MYCN, S100B, TCF4	93,032	51	CL:0000451	
Average DC	Default assignment by BRAQUE	NA (≥70%);	AXL, BCL6, CD31, CD56, CD74, CLEC9A, CLEC10A, MYC, OX40, TIM3	CD14, CD11c, CD45, CD68, CD86, CD141, CD163, CD207, cMAF, HLADR, ID2, IDO, IRF8, LYZ, MX1, MYCN, PRDM1, PU1, PDL1	CD1A, CD1c, CD7, CD16, CD103, CD303, IRF4, TCF4	**CD207, TIM3**	57,998	6		
ID2+ Ki-67+ B cells	ID2+ Proliferating B cells (from BRAQUE2 on DC)	follicular (50-70%); interstitial (20-50%)	BCL6, ID2, Ki-67, MX1	CD45, CD303	CD74, PRDM1	BCL6, CD11c, ID2, Ki-67	5,023	8		
Macrophages	Tissue macrophages (from BRAQUE2 on DC)	medullary cords (50-70%); paracortex (20-50%)		LYZ	CD11c, CD303, CLEC10A	CD11c, CD163, IRF8, PU1	40,100	47		
Monocytes	Monocytes (from BRAQUE2 on DC)	interstitial (50-70%);				BCL6, CD5, CD7, CD11c, CD31, CD86, CD303, CLEC9A, CLEC10A, ID2, IRF8, LYZ, PU1	39,288	12	CL:0000576	[81]
Myeloid									CL:0000763	
monocytes	Monocytes	interstitial (50-70%);	LYZ, PU1	CD14, CD45, CD86	CD11c, CD74, MYC, TIM3	AXL, BCL2, CD7, CD14, CD86, cMAF, LYZ	95,970	30	CL:0000576	[81]
CD16+ macs	CD16+ macrophages	sinusoidal NOS (50-70%);	AXL, CD4, CD16, CD31, CD163, TIM3	CD45, CD86, cMAF, MX1	BCL2, CD11c, CD68, MYC, MYCN, PDL1	AXL, CD16, CD163, LYZ	16,979	15		[57, 140]

CD16+ monos	CD16+ alternative monocytes	interstitial, medullary cords, sinusoidal NOS (20-50%)	CD16, CD31	BCL2, CD45, MX1, MYC	AXL, CD11c, CD86, MYCN, TIM3	AXL, BCL2, CD11c, CD14, CD16, CD45, CD103, LYZ	9,730	6	CL:0002397	[57, 140]
CD7/23/GZMB Myelo	Activated macrophages	Activation spot (≥70%);	CD7, CD23, GZMB, IDO	CD103, MX1	AXL, CD14, CD74, CD86, MYC	CD7, CD16, CD23, CD68, GZMB	86,575	44		[93, 95, 141, 142]
GZMB+	GZMB+ cells	Activation spot (50-70%);	GZMB	CD23, CD45, IRF8	CD4, CD74, CD86, IDO, MYC	CD14, CD74, GZMB, HLADR, Lyve1, MX1	4,730	8		[93, 141]
phagocytes CD68+	CD68+ phagocyting macrophages (also tingible body macrophages)	interstitial (50-70%); paracortex (20-50%)	CD11c, CD68, CD74, CD86, MYC, PDL1	CD4, CD45, HLADR, LYZ, PU1, TIM3	AXL, BCL2, CD10, CD31, CD163, cMAF, ID2, MX1, MYCN	**CD68, CD163**	30,714	20	CL:0000888	[81, 140, 143]
GC macs	GC macrophages	follicular (≥70%);	CD11c, CD45, CD68, CD86, HLADR, ID2, IRF8, PU1	CD10, cMAF, Ki-67, MYC	CD23, CD74, PDL1	**CD11c, CD68, CD86**	5,189	6		
Macrophages	Resident tissue macrophages	medullary cords (50-70%); paracortex (20-50%)	CD4, CD163	BCL2, CD68, TIM3	AXL, CD14, CD31, CD45	CD163, cMAF, LYZ, PU1	140,103	29	CL:0000235	[140, 143]
Lyve1+ sinus Macs	Lyve1+ perivascular macrophages	sinusoidal NOS (≥70%);	AXL, CD31, Lyve1	CD163, cMAF, MYC	CD4, CD11c, CD14, MX1, MYCN, TIM3	CD14, CD163, cMAF, Lyve1, LYZ	96,071	46	CL:0000887	[140]
Lyve1+ CD16+ sinus Macs	CD16+ Lyve1+ perivascular macrophages	sinusoidal NOS (≥70%);	AXL, CD4, CD11c, CD16, CD31, CD163, Lyve1, MX1	MYC, MYCN, TIM3	CD14, CD45, CD86, cMAF	CD16, CD23, Lyve1	27,410	15	CL:0000887	[140]
Neutrophils	Neutrophils	interstitial, paracortex, medullary cords, sinusoidal NOS (20-50%)	CD10, CD16, CD86, LYZ, PU1	CD45		CD10, CD14, CD16, LYZ	11,116	7	CL_0000775	[81]
Act Macs	Activated macrophages	paracortex, capsular (20-50%)	MYC, TIM3	CD4, CD74, CD86, HLADR, IDO	BCL2, CD11c, CD23, CD31, CD45, CD103, CD163, GZMB, ID2, IRF8, MX1, MYCN, PDL1	CD10, CD11c, CD16, cMAF, MX1, PDL1	33,633	15		[81]

PU1 cMAF	PU1+ macrophages	interstitial (50-70%); paracortex (20-50%)	CD163, cMAF, PU1	AXL, CD11c, CD45, CD68, CD74, CD86, HLADR, MYC, MYCN, TIM3	BCL2, CD4, ID2	**cMAF, PU1**	27,984	10		
Myeloid undefined	Myeloid cells of undefined phenotype	interstitial, paracortex (20-50%)	MYC	AXL, BCL2, CD31, CD74, CD103, cMAF, ID2, MX1, TIM3	CD4, CD10, CD45, CD68, CD86, CD163, MYCN	CD10, CD11c, CD14, cMAF, IRF8, Lyve1, LYZ, MYCN, PDL1	23,879	14		
Average Myeloid	Default assignment by BRAQUE	NA (≥70%);	HLADR, TIM3	AXL, CD7, CD10, CD11c, CD14, CD16, CD23, CD68, CD74, CD86, cMAF, GZMB, ID2, IDO, MX1, MYC, PDL1, PU1	CD4, CD31, CD45, CD103, IRF8, Ki-67, Lyve1, LYZ, MYCN	CD163, LYZ	53,097	6		
Stromal Cells									CL:0000057	
endothelium	Endothelial cells	diffuse, interstitial and extranodal	CD14, CD31, CD34, CD64, SOX9, TCF4	AID, AXL, CD141, CD248, MYC, PNAd, vWF, ZEB1	CD137, CD207, CD23, CD56, CD68, CLEC10A, cMAF, CXCL13, GZMB, MX1, OX40, PD1, PDPN, TIM3	CD16, CD3, CD34, CD4, HLADR, vWF	167,539	74	CL:0000071	[61, 144-146]
HEV	PNAd+ endothelial cells	paracortex; intranodal	CD248, CD31, CD34, CD64, PNAd	AID, CD14, CD141, MYC, PD1, SOX9, TCF4, vWF	AXL, CD137, CD23, CD303, CD56, CD86, CLEC10A, CLEC9A, CXCL13, GZMB, LYZ, MX1, MYCN, OX40, PDL1,	CD3, CD31, CD34, CD4, Ki-67, PAX5, PNAd, PU1	54,324	27	UBERON:8410038	[146]

					PDPN, TIM3, TOX1, ZEB1					
Lyve1+ endothelium	Lyve1+ lymphatic endothelium	medullary cords sinusoidal lining and extranodal	AXL, CD163, CD303, CD31, CD64, cMAF, Lyve1, ZEB1	AID, CD14, CXCL13, LYZ, TCF4	CD137, CD4, CD68, lambda, MX1, MYC, MYCN, SOX9, TIM3, vWF	CLEC9A, Lyve1, TCRd, vWF	59,949	26	CL:0002138	[146]
stroma (extranodal)	non-endothelial stromal cells in the perinodal space	extranodal	BCL6, cMAF, ZEB1	AXL, CD248, CD34, TCRd	CD10, CD207, CD303, CD56, MYC, PDPN, S100B, TCF4	CD16, FOXP3, IRF8, MYCN, PU1, S100B, ZEB1	48,707	50		
perifollicular stroma	non-endothelial stromal cells delimitating the B cell follicles	paracortical crowding around the B cell follicles	CD11c, CD14, CD141, TIM3	CXCL13, MYC, ZEB1	CD1c, CD248, CD303, CD31, CD64, CD74, CD79a, CLEC9A, cMAF, IgD, OX40, PAX5, PNAd, PDPN, SOX9	CD14, CD141, CD206, CD31, CD79a, PNAd	70,458	11		
stromal cells	non-endothelial stromal cells (fibroblasts, myofibroblasts, FRC, smooth muscle cells)	diffuse, interstitial	AID, AXL, CD248, CD34, CD5, CD56, CD64, CLEC10A, MYC, PNAd, SOX9, TCF4	CD103, CD137, CD21, CD23, CD31, CD74, cMAF, GZMB, MX1, PD1, TOX1	CD11c, CD14, CD303, CD68, CD7, EOMES, IDO, LAG3, Lyve1, PDPN, TIM3, ZEB1	**AXL**	277,535	100		[60, 81]
stromal cell MYC+	MYC+ non-endothelial stromal cells (fibroblasts, myofibroblasts, FRC, smooth muscle cells)	diffuse, interstitial	AID, AXL, CD137, CD14, CD207, CD23, CD248, CD31, CD34, CD56, CD64, CLEC10A, cMAF, CXCL13, GZMB, MYC,	CD10, CD11c, CD141, CD69, TIM3, TOX1	CD103, CD1c, CD21, CD7, LYZ, MX1, PDL1, PRDM1	CD206, CD248, vWF	37,622	25		[60]

	OX40, PD1, PNAd, PDPN, SOX9, TCF4, ZEB1							
FDC subpop	BCL6, CD21, CD23, CD4543, CD74, CD79a, CD86, CXCL13, PAX5, PD1, PDPN, TOX1	CD20, GZMB	AID, CLEC10A, IgD, LAG3, MX1, MYC, MYCN, PRDM1, PU1, SOX9	**CD21, CD23, CD248, PNAd**	4,071	5	CL:0000442	[81]

	Markers frequency in cell-type defined clusters					
	70-100%	**50-69%**	**30-49%**	**Markers ranked 1st-5th**	**n. cells**	**n. clusters**
CD4						
TCF7lo		CD86, FOXP3, IRF4, PRDM1, TIM3, TOX1	BCL6, CD23, CD30, CD56, CD69, CD137, cMAF, GATA3, GZMB, ID2, MX1, MYC, OX40, PD1	**FOXP3**	98871	80
TCF7hi	TCF7	GATA3	BCL6, CD30, CD69, CD137, GZMB, ID2, MYC, PD1, PRDM1	CD86, Ki-67, S100B, TCF7	263772	50

TCF7avg		CD69, TIM3	CD23, CD56, CD86, cMAF, CXCL13, GATA3, ID2, IRF4, MX1, MYC, OX40, PD1, PDL1, PRDM1, TOX1	FOXP3, HLADR	331053	158
CD8						
TCF7lo			CD69, CD74, GZMB, PD1, TIM3, TOX1	CD103, cMAF, EOMES, S100B	35068	58
TCF7hi	TCF7		BCL6, CXCL13, GATA3, MYC, PRDM1	CD56, CD86, cMAF, RORC, TCF7	31864	46
TCF7avg			CD86, CXCL13, OX40, PRDM1, TIM3	HLADR	92313	92